

RESEARCH ARTICLE | FEBRUARY 25 2025

Ab initio spin-mapping non-adiabatic dynamics simulations of photochemistry

Special Collection: [Algorithms and Software for Open Quantum System Dynamics](#)

Braden M. Weight  ; Arkajit Mandal  ; Deping Hu  ; Pengfei Huo 

 Check for updates

J. Chem. Phys. 162, 084105 (2025)

<https://doi.org/10.1063/5.0248950>

 CHORUS



Articles You May Be Interested In

KoopmanLab: Machine learning for solving complex physics equations

APL Mach. Learn. (September 2023)

Experimental realization of a quantum classification: Bell state measurement via machine learning

APL Mach. Learn. (September 2023)

Ab initio spin-mapping non-adiabatic dynamics simulations of photochemistry

Cite as: J. Chem. Phys. 162, 084105 (2025); doi: 10.1063/5.0248950

Submitted: 14 November 2024 • Accepted: 2 February 2025 •

Published Online: 25 February 2025



View Online



Export Citation



CrossMark

Braden M. Weight,^{1,a)} Arkajit Mandal,^{2,b)} Deping Hu,³ and Pengfei Huo^{4,5,6,c)}

AFFILIATIONS

¹ Department of Physics and Astronomy, University of Rochester, Rochester, New York 14627, USA

² Department of Chemistry, Texas A & M University, College Station, Texas 77842, USA

³ Center for Advanced Materials Research, Beijing Normal University, Zhuhai 519087, China

⁴ Department of Chemistry, University of Rochester, Rochester, New York 14627, USA

⁵ The Institute of Optics, Hajim School of Engineering, University of Rochester, Rochester, New York 14627, USA

⁶ Center for Coherence and Quantum Optics, University of Rochester, Rochester, New York 14627, USA

Note: This paper is part of the JCP Special Topic on Algorithms and Software for Open Quantum System Dynamics.

^{a)}E-mail: bweight@ur.rochester.edu

^{b)}E-mail: mandal@tamu.edu

^{c)}Author to whom correspondence should be addressed: pengfei.huo@rochester.edu

ABSTRACT

We perform on-the-fly non-adiabatic molecular dynamics simulations using the recently developed spin-mapping formalism. Two quantum dynamics approaches based on this mapping formalism, (i) the fully linearized Spin-LSC and (ii) the partially linearized Spin-PLDM, are explored using the quasi-diabatic propagation scheme. We have performed dynamics simulations in four *ab initio* molecular models for which benchmark *ab initio* multiple spawning (AIMS) data have been published. We find that the spin-LSC and the previously reported symmetric quasi-classical (SQC) approaches provide nearly equivalent population dynamics. While we expected the more involved spin-PLDM method to provide superior accuracy compared to the other mapping-based approaches, SQC and spin-LSC, we found that it performed with equivalent accuracy compared to the AIMS benchmark results. We further explore the underpinnings of the spin-PLDM correlation function by decomposing its N^2 density matrix-focused initial conditions, where N is the number of states in the quantum subsystem. Finally, we found an approximate form of the spin-PLDM correlation function, which simplifies the simulation and reduces the computational costs from N^2 to N .

Published under an exclusive license by AIP Publishing. <https://doi.org/10.1063/5.0248950>

25 February 2025 14:17:03

I. INTRODUCTION

Simulating non-adiabatic dynamics of realistic molecules using *ab initio* on-the-fly techniques has been one of the central topics of theoretical chemistry over the past few decades.^{1–38} Performing on-the-fly dynamics requires two major tasks: (i) accurate electronic structure and (ii) propagation of the correlated electron–nuclear dynamics.³⁹ Due to the size of the total Hilbert space needed to perform an exact, full-dimensional quantum simulation, various approximated quantum dynamics approaches are needed. The most successful and computationally accessible methods are the mixed quantum–classical (MQC) approaches such as the fewest switches surface hopping (FSSH)¹ and the mean-field Ehrenfest approach.⁴⁰

These approaches rely on the output of the electronic structure methods to evolve the electronic subsystem quantum mechanically while treating the nuclear subsystem classically.³² Unfortunately, the MQC approximation introduces some known drawbacks, notably the breakdown of detailed balance,⁴¹ the artificial creation of electronic coherence,¹⁸ or incorrect chemical kinetics.¹⁸

In addressing these known limitations, non-adiabatic dynamics approaches continue to be developed^{30,35,36,42–49} in order to systematically improve the accuracy of results while retaining a similar level of computational cost. Most notably, a lot of trajectory-based methods in the diabatic representation have been developed, including partial linearized density matrix^{7,50} (PLDM), state-dependent ring polymer molecular dynamics,^{13,15,23,51–54} quantum–classical path

integral (QCPI) approach,^{55–58} the quantum classical Liouville equation (QCLE) dynamics,^{14,59} and the symmetric quasi-classical (SQC) approach^{11,12,60–62} with trajectory-specific zero-point energy.²⁷ Even more recently, the spin-mapping formalism^{28,63–66} has been shown to provide a substantial increase in accuracy in non-adiabatic benchmark systems, such as the Fenna–Matthews–Olson (FMO) complex, the spin-boson models,^{28,63–65} as well as others.^{67–69} Another related approach is the generalized discrete truncated Wigner approximation (GDTWA).⁷⁰ A recent connection between the popular FSSH and mapping approaches has recently been developed and tested in both model and *ab initio* settings, which is the mapping approach to surface hopping (MASH).^{71–74}

The spin-mapping approaches build upon the idea of mapping the electronic Hilbert space to one of different types. For example, the Meyer–Miller–Stock–Thoss (MMST) mapping relations, employed in the development of the SQC²⁷ and PLDM⁷ approaches, rely on mapping the N electronic states to that of a set of N quantum harmonic oscillators, of which each is projected to include only their ground and first excited states.^{75–77} One of the main drawbacks of this mapping is that the Hilbert space of the quantum harmonic oscillator is larger than that of the original electronic system and so requires projection or the normalization of the population to restrict the dynamics to these DOFs. However, the spin-mapping formalism instead is able to map the operators in the Hilbert space of N -levels, onto functions of the $SU(N)$ Lie group that precisely preserve the original symmetry of the N -level system (i.e., generalized Bloch spheres).^{28,63,66} By construction, the normalization of the *total* population is guaranteed to be unity for all time since the radius of the hyper-sphere of the mapping variables is fixed. In Ref. 66, it was shown that the spin-linearized semi-classical (LSC) approach^{28,63} almost perfectly reproduced the quantum mechanically exact dynamics of model conical intersection systems and outperformed both Ehrenfest dynamics and the surface hopping approach. It is thus natural to apply the diabatic spin-LSC and related method to perform on-the-fly simulations if one can easily interface these diabatic trajectory-based approaches and the adiabatic electronic structure information.

In our recent studies, we have developed and implemented the quasi-diabatic (QD) propagation scheme^{78–84} to seamlessly combine adiabatic electronic structure methods with diabatic quantum dynamics methods. The QD scheme relies on a short-time reference nuclear geometry (whose electronic states are often called “crude adiabatic” states), which is a set of locally diabatic states (due to their fixed characters associated with the reference geometry) and acts like a “complete basis” during a short time nuclear propagation time step (when the nuclear DOF is still close to the reference geometry). After this short-time propagation, the QD states are updated to the new reference geometry. In this propagation scheme, one does not construct a global diabatic representation but uses a sequence of local diabatic representations for each short-time segment to propagate quantum dynamics. Note that the quasi-diabatic propagation scheme^{78–82} should not be confused with the approximate diabatic representation, which is also often referred to as the “QD” representation in the literature.^{85–87}

In this work, we use the QD propagation scheme to seamlessly combine the recently formulated spin-mapping quantum dynamics methods^{28,63–66} with the adiabatic output of the state-averaged complete active space self-consistent field (SA-CAS-SCF)

electronic structure method. Here, we perform a direct on-the-fly non-adiabatic dynamics simulation to investigate the population dynamics of various photo-excited species: ethylene, fulvene, methyliminium cation (CH_2NH_2^+), and 1,2-dithiane, of which all have been previously investigated using the higher-level, wavepacket-based *ab initio* multiple spawning (AIMS) approach.^{73,88–90} The AIMS results are interpreted as a benchmark for the trajectory-based methods in this work. We note that AIMS itself is not exact⁷³ and sometimes difficult to converge (see the Appendix) and that it is only used as a measure of overall performance for the MQC approaches used in this work. These *ab initio* molecular systems provide a set of benchmarks that explore various phenomena found in non-adiabatic dynamics, such as electronic avoided crossings and conical intersections, in a simplified way and offer a direct connection between the commonly used model systems of Tully and realistic, *ab initio* molecules.^{83,88}

While we expected the more involved spin-PLDM method to provide superior accuracy compared to the other mapping-based approaches, SQC and spin-LSC, we found that it performed with equivalent accuracy compared to the AIMS benchmark results. We further explored the nature of the spin-PLDM correlation function by examining the various components individually. Here, we found that an approximate scheme can be constructed to give results of similar accuracy to the full spin-PLDM correlation function, where one only needs to calculate a single column of the N^2 initial conditions, which includes the initially excited population element. This reduces the computational expense from N^2 trajectory-converged simulations to N simulations, still amounting to more computations than the spin-LSC approach, which only ever requires a single trajectory-converged calculation for the initial conditions used in this work. These simulations provide valuable tests of the numerical performance of various non-adiabatic approaches beyond model systems, which have been used as the main workhorse for benchmarking new methods in the field of quantum dynamics. It is our hope that these benchmark studies using realistic, *ab initio* systems will help foster the development of new quantum dynamics approaches.

II. THEORY

A. The molecular Hamiltonian

Simulating quantum dynamics of molecular systems amounts to solving the coupled electron–nuclear dynamics governed by the molecular Hamiltonian,

$$\hat{H} = \hat{T}_{\mathbf{R}} + \hat{T}_{\mathbf{r}} + \hat{V}_{\text{c}}(\mathbf{r}, \mathbf{R}) \equiv \hat{T}_{\mathbf{R}} + \hat{H}_{\text{el}}(\mathbf{r}, \mathbf{R}), \quad (1)$$

where $\hat{T}_{\mathbf{R}} = -\frac{\hbar^2}{2M} \nabla_{\mathbf{R}}^2$ and $\hat{T}_{\mathbf{r}} = -\frac{\hbar^2}{2m_e} \nabla_{\mathbf{r}}^2$ are the kinetic energy operators for the nuclear and electronic degrees of freedom (DOF), respectively, $\hat{V}_{\text{c}}(\mathbf{r}, \mathbf{R})$ describes the Coulomb interactions between all DOF (electronic and nuclear), and $\hat{H}_{\text{el}}(\mathbf{r}, \mathbf{R}) = \hat{T}_{\mathbf{r}} + \hat{V}_{\text{c}}(\mathbf{r}, \mathbf{R})$ is the electronic part of the molecular Hamiltonian. Directly simulating quantum dynamics by solving the time-dependent Schrödinger equation (TDSE) governed by \hat{H} remains intractable. Instead, mixed-quantum classical and semi-classical quantum dynamics approaches offer an efficient but approximate solution to the TDSE. These approaches solve the quantum dynamics in the following two steps.

For most of the on-the-fly methods, the task of quantum dynamics propagation is decomposed into two steps. In the first step, an electronic structure calculation is performed to obtain adiabatic potential energies and gradients. That is, one solves the time-independent Schrödinger equation for the electronic part of the Hamiltonian,

$$\hat{H}_{\text{el}}(\mathbf{r}, \mathbf{R})|\epsilon_{\mu}(\mathbf{R})\rangle = \epsilon_{\mu}(\mathbf{R})|\epsilon_{\mu}(\mathbf{R})\rangle, \quad \mathbf{R} \in \{R_a\}, \quad (2)$$

where $|\epsilon_{\mu}(\mathbf{R})\rangle$ and $\epsilon_{\mu}(\mathbf{R})$ are referred to as the *adiabatic* states and *adiabatic* potential energy surfaces, respectively.

In the second step, one evolves the electronic and nuclear degrees of freedom (DOFs), governed by the total Hamiltonian \hat{H} , using the output of the previous step. The total Hamiltonian \hat{H} in the adiabatic representation can be written as

$$\hat{H} = \sum_a \frac{\left(\hat{P}_a - i\hbar\hat{d}(R_a)\right)^2}{2M_a} + \sum_{\mu} \epsilon_{\mu}(\mathbf{R})|\epsilon_{\mu}(\mathbf{R})\rangle\langle\epsilon_{\nu}(\mathbf{R})|, \quad (3)$$

where $d_{\mu\nu}(\mathbf{R}) = \langle\epsilon_{\mu}(\mathbf{R})|\nabla_a|\epsilon_{\nu}(\mathbf{R})\rangle$ is the nonadiabatic coupling vector (NACV), which originates from the nuclear kinetic energy operator $\hat{T}_{\mathbf{R}}$ and appears due to the dependence of the adiabatic states on the nuclear coordinates. The matrix elements [note that diagonal elements are zero, $d_{\mu\mu}(R_a) = 0$] of the NACV can also be expressed as

$$d_{\mu\nu}(R_a) = \frac{\langle\epsilon_{\mu}(\mathbf{R})|\nabla_a\hat{H}_{\text{el}}|\epsilon_{\nu}(\mathbf{R})\rangle}{\epsilon_{\nu}(\mathbf{R}) - \epsilon_{\mu}(\mathbf{R})}, \quad \mu \neq \nu, \quad (4)$$

where the denominator becomes zero at conical intersections or trivial crossings [i.e., $\epsilon_{\nu}(\mathbf{R}) - \epsilon_{\mu}(\mathbf{R}) = 0$]. Furthermore, NACV is often very sharp (in nuclear coordinate space), requiring a small time step to obtain reasonable dynamics.⁸¹ Performing dynamics using \hat{H} given in Eq. (3) thus becomes numerically challenging.

Barring this numerical challenge, importantly the adiabatic representation also introduces incompatibility challenges for propagating the coupled electronic and nuclear degrees of freedom. This is because many quantum dynamics approaches, such as the spin-mapping approaches used in this work,^{28,66} are instead formulated in the diabatic representation $\{|\mu\rangle\}$. Reformulating these methods from diabatic to adiabatic representations requires additional theoretical efforts.⁶⁰ Within the diabatic representation $\{|\mu\rangle\}$, however, the NACVs (and, by extension, the second derivative couplings) vanish by definition,

$$\langle v|\nabla_a|\mu\rangle = 0, \quad (5)$$

as the diabatic states $|\mu\rangle$ are independent of the nuclear configuration $\{\mathbf{R}\}$ and are only defined based on their character. Meanwhile, diabatic states are not unique and are often not routinely available. The total molecular Hamiltonian in the diabatic representation has the following preferable compact form:

$$\hat{H}_{\text{D}} = \sum_a \frac{\hat{P}_a^2}{2M_a} \otimes \hat{\mathcal{I}} + \sum_{\mu\nu} V_{\mu\nu}(\mathbf{R})|\mu\rangle\langle\nu|, \quad (6)$$

where $\hat{\mathcal{I}}$ is the identity operator in the electronic subspace and $V_{\mu\nu}(\mathbf{R}) = \langle v|\hat{H}_{\text{el}}(\mathbf{r}, \mathbf{R})|\mu\rangle$ has off-diagonal matrix elements

(called diabatic coupling) in contrast to its adiabatic counter-part $\sum_{\mu} \epsilon_{\mu}(\mathbf{R})|\epsilon_{\mu}(\mathbf{R})\rangle\langle\epsilon_{\mu}(\mathbf{R})|$ in Eq. (3). In this work, we use the quasi-diabatic (QD) framework^{82,83} to directly propagate the quantum dynamics using the outputs obtained in the adiabatic representation. Below, we briefly describe the spin-mapping approaches^{28,66} and how to interface them with adiabatic electronic quantities $\epsilon_{\mu}(\mathbf{R})$, $\nabla_{R_a}\epsilon_{\mu}(\mathbf{R})$, $d_{\mu\nu}(R_a)$, and $\{|\epsilon_{\mu}(\mathbf{R})\rangle\}$ using the QD framework.

B. The spin-mapping approach

In this work, we closely followed the spin-mapping (SM) approach of Richardson and co-workers.^{28,63–65} In particular, we will use both the spin-linearized semi-classical (spin-LSC) approximation^{28,66} and spin partially linearized density matrix (spin-PLDM) approach^{64,65} to perform quantum dynamics. A detailed discussion of the SM representation and the $SU(N)$ Lie group can be found in Ref. 66. Consider the coupled electron–nuclear diabatic Hamiltonian with the electronic operators split into state-independent $V_0(\hat{\mathbf{R}})$ and state-dependent $\hat{V}(\hat{\mathbf{R}})$ terms,

$$\hat{H} = \hat{T}_{\mathbf{R}} + V_0(\hat{\mathbf{R}}) + \hat{V}(\hat{\mathbf{R}}), \quad (7)$$

where the trace over the electronic subsystem $\text{Tr}_{\text{e}}[\hat{V}(\hat{\mathbf{R}})] = 0$ by construction. Note that $\hat{V}(\hat{\mathbf{R}})$ is an $N \times N$ matrix, where N is the number of considered electronic states.

Many dynamical quantities of interest can be written as a two-time correlation function,

$$C_{AB}(t) = \text{Tr}[\hat{\rho}_n(0)\hat{A}(0)\hat{B}(t)], \quad (8)$$

where $\hat{A}(0)$ and $\hat{\rho}_n(0)$ can be interpreted as the factorized initial electronic and nuclear configurations for the system at $t = 0$ and $\hat{B}(t) = e^{i\hat{H}t/\hbar}\hat{B}e^{-i\hat{H}t/\hbar}$. In this work, we take \hat{A} and \hat{B} to be operators in the $N \times N$ electronic sub-space (population and coherence), $\hat{\rho}_n$ is the nuclear density operator, and the trace is over both nuclear and electronic degrees of freedom (DOFs).

1. Spin-LSC

In the fully linearized spin-mapping framework, any electronically, two-operator correlation function can be written as

$$C_{AB}(t) = \langle \mathcal{A}_{\text{w}}(\mathcal{Z}(0)) \mathcal{B}_{\text{w}}(\mathcal{Z}(t)) \rangle, \quad (9)$$

where \mathcal{A}_{w} and \mathcal{B}_{w} are the Stratonovich–Weyl (SW) transforms of the operators \hat{A} and \hat{B} , respectively, under the w-representation,

$$[\hat{A}]_{\text{w}}(\mathcal{Z}, 0) \equiv \mathcal{A}_{\text{w}}(\mathcal{Z}(0)) = \text{Tr}_{\text{e}}[\hat{A} \hat{\omega}_{\text{w}}^{\dagger}(\mathcal{Z}(0))], \quad (10a)$$

$$[\hat{B}]_{\text{w}}(\mathcal{Z}, t) \equiv \mathcal{B}_{\text{w}}(\mathcal{Z}(t)) = \text{Tr}_{\text{e}}[\hat{B} \hat{\omega}_{\text{w}}(\mathcal{Z}(t))]. \quad (10b)$$

In the above-mentioned transform, the SW kernel with the w-representation^{28,66} can be written as

$$\hat{\omega}_{\text{w}}(\mathcal{Z}, t) = \frac{1}{2} \sum_{\mu, \nu}^N (\mathcal{Z}_{\mu}(t) \mathcal{Z}_{\nu}^*(t) - \gamma_{\text{w}} \delta_{\mu\nu}) |\mu\rangle\langle\nu|, \quad (11)$$

in the electronic basis $\{|\mu\rangle\}$ (in the diabatic representation). The kernel is evaluated as a function of the complex-valued, time-evolved

mapping variables $\mathcal{Z} = \{\mathcal{Z}_1, \mathcal{Z}_2, \dots, \mathcal{Z}_N\}$ with a fixed zero-point energy parameter (for the w-representation),^{28,66}

$$\gamma_w = \frac{2}{N}(\sqrt{N+1} - 1), \quad (12)$$

where N is the total number of states considered in the quantum subsystem. One can identify that^{28,66}

$$\mathcal{Z}_\mu = q_\mu + i p_\mu, \quad (13)$$

where q_μ and p_μ are equivalent to the commonly used MMST mapping variables. However, the explicit use of the MMST mapping variables is not required in the current work and thus not used in the implementation of this work.

The correlation function in Eq. (9) is evaluated using focused initial conditions^{28,66} such that

$$\langle \dots \rangle = \sum_{\lambda}^N \int d\mathbf{R} d\mathbf{P} d\mathcal{Z} \cdot \rho_n(\mathbf{R}, \mathbf{P})(\dots) \cdot \rho_w^{(\lambda)}, \quad (14)$$

where $\rho_n(R, P)$ is the nuclear Wigner distribution and $\rho_w^{(\lambda)}$ is the focused initial electronic distribution, which is expressed as follows:

$$\rho_w^{(\lambda)} = \frac{\delta(|\mathcal{Z}_\lambda|^2 - \gamma_w - 2)\Pi_{\mu \neq \lambda}\delta(|\mathcal{Z}_\mu|^2 - \gamma_w)}{\int d\mathcal{Z}\delta(|\mathcal{Z}_\lambda|^2 - \gamma_w - 2)\Pi_{\mu \neq \lambda}\delta(|\mathcal{Z}_\mu|^2 - \gamma_w)}. \quad (15)$$

This spin-LSC correlation function using the focused initial conditions [Eq. (14)] is evaluated by averaging over an independent set of trajectories, one for each λ in the sum in Eq. (14). For each λ , the mapping variables \mathcal{Z} are initialized as

$$\mathcal{Z}_\lambda = \sqrt{2 + \gamma_w} \cdot e^{i\phi_\lambda}, \quad (16a)$$

$$\mathcal{Z}_\mu = \sqrt{\gamma_w} \cdot e^{i\phi_\mu}, \quad \mu \neq \lambda, \quad (16b)$$

where \mathcal{Z}_λ is for the initially focused state and $\{\phi\}$ is a random angle sampled between 0 and 2π , independently from one another.

In this work, we are only interested in correlation functions with $\hat{A}(0) = |\sigma\rangle\langle\sigma|$ (i.e., the initial condition), which indicates that the initial electronic density matrix is a single electronic state σ . This is the case for a time-independent Frank–Condon excitation, often used as the initial condition for non-adiabatic dynamics studies. In this case, the spin-LSC correlation function, for the focused sampling in Eq. (14), is greatly simplified to

$$C_{|\sigma\rangle\langle\sigma|B}(t) = \int d\mathbf{R} d\mathbf{P} d\mathcal{Z} \rho_b(\mathbf{R}, \mathbf{P}) \rho_w^{(\sigma)} B_w(\mathcal{Z}, t). \quad (17)$$

This is because the SW transform of \hat{A} results in

$$A_w = [|\sigma\rangle\langle\sigma|]_w = \delta_{\sigma\lambda} \quad (18)$$

and thus picks out a single term in Eq. (14). Since there is no sum over λ in the correlation function, one only needs to converge one set of trajectories [$\lambda = \sigma$ in Eq. (15)], which involves sampling the mapping variables as $\mathcal{Z}_\sigma(0) = \sqrt{2 + \gamma_w}e^{i\phi_\sigma}$ and $\mathcal{Z}_{\mu \neq \sigma}(0) = \sqrt{\gamma_w}e^{i\phi_\mu}$. Still, one must still ensure that both the random phases $\{\phi\}$ of the mapping variables and the nuclear phase space variables $\{\mathbf{R}, \mathbf{P}\}$

are sufficiently converged/sampled. For computing, for example, reaction rate constants (with the flux-side correlation function)⁹¹ or optical response functions,^{92,93} which require the initial density matrix to be off-diagonal (i.e., $\hat{A} \neq |\sigma\rangle\langle\sigma|$), one needs to explicitly perform the sum.

The propagation of the mapping and nuclear variables can be done in the usual MMST manner as

$$\frac{d\mathcal{Z}_\mu}{dt} = -i \sum_v \langle \mu | \hat{V}(\mathbf{R}) | v \rangle \mathcal{Z}_v, \quad (19a)$$

$$\frac{dR}{dt} = \frac{P}{M}, \quad (19b)$$

$$\frac{dP}{dt} = F_0(\mathbf{R}) + \mathcal{F}_e(\mathbf{R}, \mathcal{Z}), \quad (19c)$$

where $F_0(\mathbf{R}) = -\nabla V_0(\mathbf{R})$ is the state-independent force, and the state-dependent forces $\mathcal{F}(\mathbf{R}, \mathcal{Z})$ are calculated as

$$\begin{aligned} \mathcal{F}_e(\mathbf{R}, \mathcal{Z}) &= -\frac{1}{2} \sum_{\mu\nu} \langle \mu | \nabla \hat{V}(\mathbf{R}) | v \rangle (\mathcal{Z}_\mu(t) \mathcal{Z}_v^*(t) - \gamma_w \delta_{\mu\nu}) \\ &= -\sum_{\mu\nu} \rho_{\mu\nu}(t) \langle \mu | \nabla \hat{V}(\mathbf{R}) | v \rangle. \end{aligned} \quad (20)$$

Finally, the estimator for the reduced density matrix of a single trajectory is simply the $\mu\nu_{\text{th}}$ element of the time-evolved SW kernel [Eq. (11)],

$$\rho_{\mu\nu}(t) = \frac{1}{2} (\mathcal{Z}_\mu(t) \mathcal{Z}_\nu^*(t) - \gamma_w \delta_{\mu\nu}), \quad (21)$$

as shown in the state-dependent force expression [Eq. (20)].

There is a very interesting observation for the spin-LSC approach: when N is very large, the ZPE correction in Eq. (12) scales as $\gamma_w \propto 1/\sqrt{N} \rightarrow 0$. This means that for the system with a very large N , the ZPE correction becomes zero, and the EOMs for spin-LSC reduce to those of Ehrenfest dynamics. It is also interesting to note that $1/\sqrt{N}$ is the relative energy variance for a general system and goes to zero under the thermodynamic limit.

2. Spin-PLDM

Following a similar line of reasoning as spin-LSC outlined above, spin-PLDM can be thought of as a natural extension to the fully linearized case of spin-LSC, now incorporating two sets of mapping variables for each electronic state. Furthermore, spin-PLDM is the extension of the original PLDM approach,^{7,50,64,65,91} which was based on the MMST mapping formalism. Compared to spin-LSC, spin-PLDM can be thought of as an extension from a wavefunction representation to a density matrix representation, where one set of mapping variables ($\{\mathcal{Z}\}$) represents the “ket” moving forward in time and the other ($\{\mathcal{Z}'\}$) represents the “bra” moving backward in time. In general, the observable can be constructed as an average of these two non-interacting paths in electronic action, only connected through simultaneous interactions with nuclear motion.^{7,50,64,65,91}

The general correlation function can be written as

$$C_{AB}(t) = \left\langle \text{Tr}_e \left[\hat{A} \hat{\omega}_w^\dagger(\mathcal{Z}', t) \hat{B} \hat{\omega}_w(\mathcal{Z}, t) \right] \right\rangle, \quad (22)$$

which has two sets of mapping variables ($\{\mathcal{Z}\}, \{\mathcal{Z}'\}$), representing the forward and backward *evolution operators* instead of the operator \hat{A} or \hat{B} ,^{64,65} which has the same strategy as the original PLDM approach.⁷ Hence, the spin-LSC and spin-PLDM utilize these SW kernels to represent two vastly different quantities in the correlation function.

Here, compared to Eq. (11) for spin-LSC, the time-evolved SW kernel is modified as^{64,65}

$$\hat{\omega}_w(\mathcal{Z}, t) = \frac{1}{2} \sum_{\mu, \nu}^N (\mathcal{Z}_\mu(t) \mathcal{Z}_\nu^*(0) - \gamma_w U_{\mu\nu}(t)) |\mu\rangle\langle\nu|, \quad (23)$$

where the time-evolution [acted upon from the left of the kernel as $\hat{\omega}_w(\mathcal{Z}, t + \Delta t) = e^{-i\hat{V}(R)\Delta t} \hat{\omega}_w(\mathcal{Z}, t)$] now evolves only a single \mathcal{Z} while also “evolving the ZPE parameter,” i.e., the parameter γ_w remains unchanged, but the identity matrix is now a time-evolving matrix $\hat{U}(t)$, which can be interpreted as a time-evolving and density-matrix-element-dependent ZPE. The ZPE matrix $\hat{U}(t)$ is evolved as

$$\hat{U}(t) = e^{-i\hat{V}(R_n)\Delta t} \cdots e^{-i\hat{V}(R_2)\Delta t} e^{-i\hat{V}(R_1)\Delta t} \mathbb{1}_N, \quad (24)$$

where $\hat{V}(R_n)$ is the state-dependent potential from Eq. (7) evaluated at a nuclear configuration R_n at time t_n , after n nuclear time steps. Note that at $t = 0$, $\hat{U}(0) = \mathbb{1}_N$, which is the identity matrix in the electronic Hilbert space with N states. For spin-LSC, $\hat{U}(t) = \mathbb{1}_N$ for all time t . Furthermore, $\hat{\omega}_w^\dagger$ is the Hermitian conjugate of $\hat{\omega}_w$, expressed as follows:

$$\hat{\omega}_w^\dagger(\mathcal{Z}', t) = \frac{1}{2} \sum_{\mu, \nu}^N (\mathcal{Z}'_\nu^*(t) \mathcal{Z}'_\mu(0) - \gamma_w \hat{U}_{\nu\mu}^*(t)) |\mu\rangle\langle\nu|. \quad (25)$$

As before, we evaluate the spin-PLDM correlation function in Eq. (22) using focused initial conditions, expressed as

$$\langle \cdots \rangle = \sum_{\lambda}^N \sum_{\lambda'}^N \int d\mathbf{R} d\mathbf{P} d\mathcal{Z} \rho_b(\mathbf{R}, \mathbf{P}) \cdots \rho_w^{(\lambda)} \rho_w^{(\lambda')}. \quad (26)$$

Note now that the spin-PLDM correlation function has picked up a second sum, which focuses the backward mapping variables to electronic state λ' . This additional sampling now impedes the same simplification that was made before for spin-LSC, even for the case when only computing initial operators $\hat{A} = |\sigma\rangle\langle\sigma|$. Now, in principle, all N^2 focused initial conditions for λ and λ' will play some role in the correlation function at time $t > 0$ no matter the choice of \hat{A} .

The mapping variables are initially sampled in the same way as for spin-LSC as follows:^{64,65}

$$\begin{aligned} \mathcal{Z}_\lambda &= \sqrt{2 + \gamma_w} \cdot e^{i\phi_\lambda}; & \mathcal{Z}_\mu &= \sqrt{\gamma_w} \cdot e^{i\phi_\mu}, \quad \mu \neq \lambda, \\ \mathcal{Z}'_{\lambda'} &= \sqrt{2 + \gamma_w} \cdot e^{i\phi'_{\lambda'}}; & \mathcal{Z}'_\mu &= \sqrt{\gamma_w} \cdot e^{i\phi'_\mu}, \quad \mu \neq \lambda', \end{aligned} \quad (27)$$

where now $\{\phi\}$ and $\{\phi'\}$ are independently and randomly sampled between 0 and 2π , and the mapping variables for different trajectories are completely independent. The time-evolution of the mapping variables is identical to Eq. (19a) for the forward and backward

DOFs, while the state-dependent nuclear force is computed identically to the standard PLDM prescription^{7,50,91} as the average over the forward and backward paths,

$$\begin{aligned} \mathcal{F}_e(\mathbf{R}, \mathcal{Z}, \mathcal{Z}') &= -\frac{1}{2} \sum_{\mu, \nu} \langle \mu | \nabla \hat{V}(\mathbf{R}) | \nu \rangle \frac{1}{2} [(\mathcal{Z}_\mu(t) \mathcal{Z}_\nu^*(t) - \gamma_w \delta_{\mu\nu}) \\ &\quad + (\mathcal{Z}'_\mu(t) \mathcal{Z}'_\nu^*(t) - \gamma_w \delta_{\mu\nu})]. \end{aligned} \quad (28)$$

Note that in Eq. (28), the time-evolved ZPE matrix $\hat{U}(t)$ [cf. Eq. (23)] does not appear, since the representation of an operator $[\nabla \hat{V}(R)]$ in this case is written as $[\nabla \hat{V}]_w(\mathcal{Z}) = \text{Tr}_e[\nabla \hat{V}(R) \hat{\omega}(\mathcal{Z})]$, with the explicit expression [see Eq. (10b)] as follows:

$$[\nabla \hat{V}]_w(\mathcal{Z}) = \frac{1}{2} \sum_{\mu, \nu} \langle \mu | \nabla \hat{V} | \nu \rangle (\mathcal{Z}_\mu(t) \mathcal{Z}_\nu^*(t) - \gamma_w \delta_{\mu\nu}), \quad (29)$$

for either \mathcal{Z} or \mathcal{Z}' mapping variables (just as in spin-LSC).

The estimator for the reduced density matrix $\rho_{\mu\nu}(t)$ at time t of a single trajectory and a single initial electronic density matrix sampling (λ, λ') [cf. Eq. (26)] can be calculated by identifying the measuring operator as, for example, $\hat{B} = |\mu\rangle\langle\nu|$. Here, we assume an initial density matrix of the form $\hat{A} = |\sigma\rangle\langle\sigma|$ (which contains only a single non-zero element, on its diagonal). However, for example, to perform linear and non-linear spectroscopies,^{92,93} a more complicated initial condition dependent on coherence elements is required. In this case, one can write down the reduced density matrix elements as

$$\begin{aligned} \rho_{\mu\nu}(t) &= \text{Tr}_e[\hat{A} \hat{\omega}_w^\dagger(\mathcal{Z}', t) |\mu\rangle\langle\nu| \hat{\omega}_w(\mathcal{Z}, t)] \\ &= \langle\sigma|\hat{\omega}_w^\dagger(\mathcal{Z}', t)|\mu\rangle\langle\nu|\hat{\omega}_w(\mathcal{Z}, t)|\sigma\rangle, \end{aligned} \quad (30)$$

where the matrix element of the kernels can be obtained from Eqs. (23) and (25). Note that this is a simple matrix multiplication and a trace of four matrices, $\text{Tr}[\hat{A} \times \hat{\omega}_w^\dagger(\mathcal{Z}', t) \hat{B} \times \hat{\omega}_w(\mathcal{Z}, t)]$, which can be done for any choice of \hat{A} and \hat{B} and accomplished on-the-fly with any standard linear algebra library alleviating the need to work out the matrix elements by hand for arbitrarily complicated initial and final matrices \hat{A} and \hat{B} .

Recall that the sum of initially focused conditions [λ and λ' from Eq. (26)] affects the distribution of the mapping variables ($\mathcal{Z}, \mathcal{Z}'$), and so, the effect of this focusing does not appear in the estimator explicitly. In addition, the meaning of a single trajectory in spin-PLDM is rather unclear, since the true correlation function depends not only on simple averaging over a statistical ensemble but also over a set of sums $\{\lambda, \lambda'\}$ that, in principle, give different dynamics compared to those focused to a different density matrix element (i.e., an initial state for both the forward and backward components). As such, we will not perform any analysis on individual trajectories from this method. Finally, we note that if γ_w is set to zero, the standard PLDM EOMs are recovered. Instead, if $\mathcal{Z} = \mathcal{Z}'$ and $\hat{U}(t) \rightarrow \mathbb{1}_N$, then spin-LSC EOMs are recovered.

C. Quasi-diabatic propagation

We briefly outline the quasi-diabatic (QD) propagation scheme used in this work to connect the spin-mapping approaches, originally formulated in the diabatic quantum representation, with the adiabatic electronic structure calculations. For more details on the QD scheme in general, we refer the reader to Refs. 78, 80, 82, and 83.

Upon performing the electronic structure calculation at the initial nuclear configuration $\mathbf{R}(0)$, one obtains the necessary adiabatic quantities: adiabatic energies $\epsilon_\mu(0)$ and nuclear gradients $\nabla_{\mathbf{R}} V_{\mu\nu}(0) = \langle \epsilon_\mu(0) | \nabla_{\mathbf{R}} \hat{H}_{el} | \epsilon_\nu(0) \rangle = \mathbf{d}_{\mu\nu} * (\epsilon_\nu(0) - \epsilon_\mu(0))$, where $\mathbf{d}_{\mu\nu} = \langle \epsilon_\mu(0) | \nabla_{\mathbf{R}} \hat{H}_{el} | \epsilon_\nu(0) \rangle / (\epsilon_\nu(0) - \epsilon_\mu(0))$; see Eq. (4). Note that the adiabatic states $|\epsilon_\nu(0)\rangle$ are adiabatic in nature because their characters are fixed and are associated with the reference geometries, $\mathbf{R}(0)$. Thus, they can be viewed as a compact set of diabatic states for a short-time propagation $t \in [0, \Delta t]$. After calculating the initial force $\mathbf{F}(0)$ in the mapping representation [Eq. (20)] and propagating the nuclear DOFs, a second electronic structure calculation is performed at the updated nuclear coordinated $\mathbf{R}(\Delta t)$ to obtain the necessary adiabatic quantities: diagonal energies $\epsilon_\mu(\Delta t)$, nuclear gradients $\nabla_{\mathbf{R}} V_{\mu\nu}(\Delta t) = \langle \epsilon_\mu(\Delta t) | \nabla_{\mathbf{R}} \hat{H}_{el} | \epsilon_\nu(\Delta t) \rangle = \mathbf{d}_{\mu\nu} \cdot (\epsilon_\nu(\Delta t) - \epsilon_\mu(\Delta t))$, and the Löwdin-orthogonalized time-overlap matrix $S_{\mu\nu}(0, \Delta t) = \langle \epsilon_\mu(0) | \epsilon_\nu(\Delta t) \rangle$; see details in Ref. 82. These adiabatic states $|\epsilon_\mu(\Delta t)\rangle$ will be used as diabatic states for quantum dynamics propagation during time $t \in [\Delta t, 2\Delta t]$. The same process will occur for the entire propagation.

The electronic mapping variables are propagated using a linearly interpolated Hamiltonian between the time 0 and Δt on the basis of adiabatic electronic states at time 0. The unitary rotation between the time Δt and time 0 bases is exactly the time-overlap matrix $S(0, \Delta t)$. Explicitly, the diagonal energies at time Δt , $[\epsilon(\Delta t)]$, are rotated to the time 0 basis as $H(\Delta t) = S(0, \Delta t) \times [\epsilon(\Delta t)] \times S^T(0, \Delta t)$, which forms a potential energy matrix that has non-zero off-diagonal elements. Here, $[\epsilon(\Delta t)]$ denotes a diagonal matrix of the adiabatic energies $\epsilon_\mu(\Delta t)$. The linearly interpolated Hamiltonian then takes the form $H(t) = [\epsilon(0)] + \frac{t-0}{\Delta t} (H(\Delta t) - [\epsilon(0)])$, where $t \in (0, \Delta t)$. The mapping variables are propagated using a velocity-Verlet scheme (by splitting the real and imaginary components of \mathcal{Z}), which solves Eq. (19a) for both spin-LSC and spin-PLDM, noting that the only difference is that the spin-PLDM contains two sets of mapping variables $\{\mathcal{Z}, \mathcal{Z}'\}$ that are propagated independently from one another. Finally, the time-evolved mapping variables $\mathcal{Z}(\Delta t)$, which are still in the time 0 basis, are rotated to the time Δt basis via the time-overlap matrix $S(0, \Delta t)$ as $S^T(0, \Delta t) \times \mathcal{Z}(\Delta t) \rightarrow \mathcal{Z}(\Delta t)$.

Furthermore, in spin-PLDM, the ZPE matrix $U(0) = \hat{1}_N$ (identity matrix at initial time) needs to be propagated according to $U(\Delta t) = \exp[-i\hat{H}\Delta t]U(0)$, which is done in the time Δt basis after the ZPE matrix has been rotated to the Δt basis such that the Hamiltonian is diagonal $[\epsilon(\Delta t)]$ and only applies a phase shift in addition to the time-overlap transformation. The stepwise ZPE matrix basis rotation and subsequent time-propagation can be compactly written as $U(\Delta t) = [e^{-i\epsilon(\Delta t)}] \times S^T(0, \Delta t) \times U(0) \times S(0, \Delta t)$.

The above-mentioned procedure is repeated for the desired number of nuclear time steps, replacing all time 0 quantities with time Δt quantities (i.e., the new reference basis) and further propagating the nuclei to acquire the time $2\Delta t$ adiabatic quantities.

D. Computational details for *ab initio* simulations

The non-adiabatic molecular dynamics simulations use an in-house-modified version^{82,83} of the SHARC non-adiabatic molecular dynamics code,⁹⁴ interfaced to the MOLPRO electronic structure package.⁹⁵ On-the-fly electronic structure calculations are performed at the level of state-averaged complete active space

self-consistent field (SA-CASSCF) approach. Ethylene, fulvene, methyliminium cation, and 1,2-dithiane were calculated with 3SA-CASSCF(2,2), 2SA-CASSCF(6,6), 2SA-CASSCF(6,5), and 3SA-CASSCF(6,4), respectively. All simulations were performed with the 6-31G* basis set. These SA-CASSCF parameters were taken from Refs. 88 and 89. In all cases, only the two lowest-energy, singlet adiabatic states, S_0 and S_1 , were used in the electronic dynamics with the initial electronic state always set to the first singlet excited state, S_1 . Unless otherwise specified, in all *ab initio* results, the time step for the nuclear propagation was 0.1 fs using 200 electronic substeps per nuclear step. Furthermore, 1000 trajectories were computed for each molecular model. To be clear, in the spin-PLDM correlation function, each initially focused electronic condition $\{\lambda, \lambda'\}$ was converged with the 1000 trajectories, in total $2 \times 2 \times 1000 = 4000$ trajectories for each of the two-state chemical models. Furthermore, to provide as much consistency between the MQC approaches as possible, the same set of 1000 initial nuclear configurations are used for each method, and for spin-PLDM, the 1000 nuclear samples were repeated for each initial electronic focusing condition.

The initial Wigner distribution is sampled from the ground vibrational state $v = 0$ on the ground electronic state $|S_0\rangle$, where the normal mode frequencies (in the harmonic approximation) are calculated based on the approach outlined in Refs. 96 and 97, as implemented in the SHARC package.⁹⁴ For all molecules, the normal mode frequencies are computed at the level of MP2/6-31++G** with the MOLPRO package, with the optimized structure obtained at the same level of electronic structure theory for the ground electronic state. In particular, the nuclear density $\rho_W(\tilde{\mathbf{R}}, \tilde{\mathbf{P}})$ in terms of the molecular normal-mode frequencies $\{\tilde{\omega}_k\}$ and phase space variables $\{\tilde{\mathbf{R}}, \tilde{\mathbf{P}}\}$ is given as⁹⁸

$$\rho_W(\tilde{\mathbf{R}}, \tilde{\mathbf{P}}) \propto \prod_{k=1}^N \exp \left[-\tanh \left(\frac{\beta \hbar \tilde{\omega}_k}{2} \right) \left(\frac{m \tilde{\omega}_k}{\hbar} \tilde{R}_k^2 + \frac{1}{m_k \tilde{\omega}_k \hbar} \tilde{P}_k^2 \right) \right].$$

The initial distribution $\{\mathbf{R}, \mathbf{P}\}$ is then obtained by transforming $\{\tilde{\mathbf{R}}, \tilde{\mathbf{P}}\}$ from the normal mode representation to the primitive coordinates using the unitary transformation that diagonalizes the Hessian matrix. The positions and momenta for all molecules were sampled from the above-mentioned Wigner distribution.

For comparison, we also use the γ -SQC- Δ approach for on-the-fly simulations. Details of it are provided in our previous work.⁸³ Where noted, we performed decoherence-corrected⁹⁹ FSSH (dTSH) as implemented in the SHARC package⁹⁴ with velocity rescaling in the direction of the velocity vector (equivalent to the “FSSH-vel” method of Ref. 73). Otherwise, we take the population trace from the studies referenced.

III. RESULTS AND DISCUSSION

Figure 1 presents the photodissociation of ethylene through its S_1/S_0 conical intersection generated by the rotation of the H-C-C-H dihedral angle. The nuclear dynamics of ethylene are analogous to the dynamics of the molecular Tully model 1,¹ as discussed in previous reports (see results for the model systems in the supplementary material).^{73,83,88} Figure 1(a) shows the popular energy-based decoherence-corrected surface hopping approach (dTSH),¹⁰⁰ which is a popular method that captures much of the decoherence that standard FSSH fails to capture. Figure 1(b)

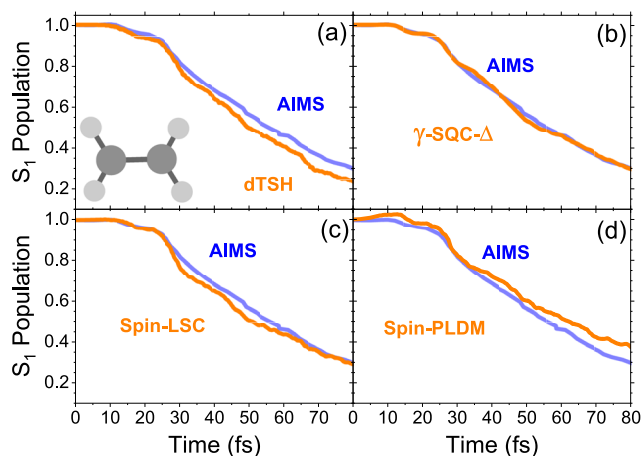


FIG. 1. S_1 population dynamics of the ethylene molecule for a variety of semi-classical methods: (a) dTSH, (b) γ -SQC- Δ , (c) spin-LSC, and (d) spin-PLDM. All methods are compared to the *ab initio* multiple spawning (AIMS) results, which are taken to be more exact compared to these semi-classical approaches. The AIMS results were taken from Ref. 73, while the dTSH results were simulated by us with the standard SHARC package.⁹⁴

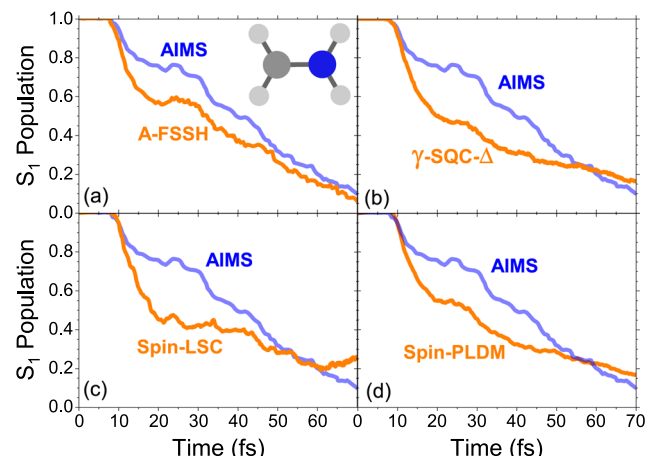


FIG. 2. S_1 population dynamics of the CH_2NH_2^+ molecule for a variety of semi-classical methods: (a) A-FFSH, (b) γ -SQC- Δ , (c) spin-LSC, and (d) spin-PLDM. All methods are compared to the *ab initio* multiple spawning (AIMS) results, which are taken to be more exact compared to these semi-classical approaches. The AIMS and A-FFSH results were taken from Ref. 89.

presents the γ -corrected SQC approach using the triangle windowing (γ -SQC- Δ). In all panels of Fig. 1, we compare the MQC approaches to the *ab initio* multiple spawning (AIMS) results taken from Ref. 73. The dTSH results were simulated by us using the standard SHARC package.⁹⁴

Figures 1(c) and 1(d) show the results from spin-LSC and spin-PLDM, respectively. At short times (less than 30 fs), all methods capture the correct population dynamics, which exhibits 10 fs of plateau followed by a short decrease and another short plateau (i.e., a shoulder). γ -SQC- Δ and spin-LSC agree with the AIMS result better than dTSH and spin-PLDM. At a longer time (more than 30 fs and less than 70 fs), dTSH and spin-LSC underestimate the population, while spin-PLDM overestimates compared to AIMS. γ -SQC- Δ shows quantitative agreement with the AIMS results. At longer times (more than 60 fs), spin-LSC matches the AIMS results, while dTSH and spin-PLDM continue to underestimate the population. Again, γ -SQC- Δ successfully matches the AIMS result. We note that while we compare our MQC simulations to the AIMS results, it is not guaranteed that the AIMS results are necessarily superior, as has been discussed in Ref. 73.

Overall, spin-PLDM seems to overestimate the population at all times. Furthermore, the initial S_1 population (between 0 and 15 fs) goes above 1.0. It should be noted that if one only considers the primary contribution to the spin-PLDM correlation function [Eq. (26)], $(\lambda, \lambda') = (\sigma, \sigma) = (1, 1)$ in this case, then the trajectory-converged population seems to be restricted to lie between 0 and 1 for all systems (see Fig. 7, discussed in more detail later). Recall that the cost of spin-PLDM scales unfavorably with the number of states N , since N^2 converged population dynamics (for each (λ, λ') initial condition): $4000 = 1000 \times 2^2$ trajectories in this case, 4× more expensive than spin-LSC, γ -SQC- Δ , and dTSH. However, as we will discuss later (in Fig. 7), a major simplification of spin-PLDM can be made by

excluding some of the N^2 initial conditions present in the full spin-PLDM correlation function. Overall, all four approaches capture the general physics of ethylene photodissociation dynamics.

Figure 2 provides a slightly more challenging system: the methyliminium cation (CH_2NH_2^+) photodynamics. This model is similar to ethylene in the sense that a CI is generated by the changing H-C-N-H dihedral angle. As such, the benchmark AIMS results suggest that the population dynamics have very similar features as the ethylene dynamics. However, a recurrence/shoulder in the population of the S_1 state appears around 25–30 fs. For this system, all methods, including augmented FSSH (A-FFSH)¹⁰¹ and the mapping approaches, overestimate the initial population transfer to the ground state around 10 fs. Following this, all approaches seem to provide a plateau in the population of the S_1 state, but only A-FFSH, γ -SQC- Δ , and spin-PLDM are able to showcase a visible recurrence in the S_1 population. Throughout the entire dynamics, A-FFSH seems to capture all the features found in the AIMS result, with spin-PLDM and γ -SQC- Δ close behind, of which both overestimate the S_1 population (or rather underestimate the population transfer rate to the ground state) at long times (more than 50 fs). For this model, it is clear that spin-LSC performs worse than the other models, while A-FFSH performs well compared to the AIMS result.

Figure 3 represents a more complicated nonadiabatic dynamics scenario in which the fulvene molecule undergoes a periodic (every ~ 10 –20 fs) and extended encounter with an S_0/S_1 CI directly linked to the stretching of the C-CH₃ stretching mode. This is similar to the Tully model No. 3,^{1,73,83,88} which exhibits a region of strong and extended coupling followed by branching and recrossing of the reflected wavepacket. At short times, all methods correctly produce a population plateau for ~ 10 fs, while spin-PLDM again exhibits a slight increase in S_1 population. At longer times, all methods exhibit vastly different results, but all capture the recurrence of the population due to the CI and subsequent second population plateau

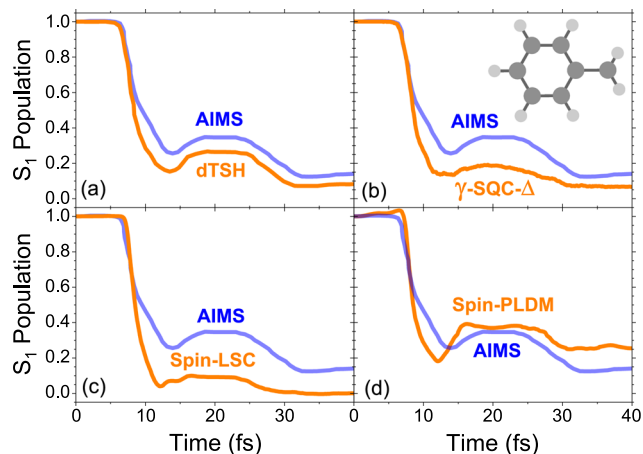


FIG. 3. S_1 population dynamics of the fulvene molecule for a variety of semi-classical methods: (a) dTSH, (b) γ -SQC- Δ , (c) spin-LSC, and (d) spin-PLDM. All methods are compared to the *ab initio* multiple spawning (AIMS) results, which are taken to be more exact compared to these semi-classical approaches. The AIMS and dTSH results were taken from Ref. 73.

(at 20 fs). All MQC approaches underestimate the S_1 population during the CI crossing at \sim 10 fs, with spin-PLDM exhibiting a larger population recurrence than the other methods before the plateau at 20 fs. Measuring the population recurrence between the minimum near 12 fs and the maximum near 20 fs, dTSH nearly quantitatively matches the AIMS result (up to a population shift) in the amount of recovered S_1 population. Spin-PLDM overestimates this population increase, while spin-LSC and γ -SQC- Δ underestimate the population increases. While none of the methods are able to reproduce the fine structure of the AIMS population, the dTSH approach is able to capture the AIMS results throughout the 40 fs more closely than the other three methods while only slightly underestimating the quantitative population.

To further probe the dynamics of fulvene, we examine the averaged nuclear density of a single nuclear DOF and a few single-trajectory properties of the spin-LSC approach. It should be noted that a single trajectory in any trajectory-based quantum dynamics approach should be understood as a fictitious observable, which is only physical upon an average over many such trajectories. However, in our experience, much can be learned about the method as well as the chemical system by examining the results/trends from a single trajectory. Such an examination helps build intuition regarding novel quantum dynamics approaches. We would also like to point out that a single trajectory in spin-PLDM is less representative than a single trajectory in any other approach since the correlation function depends on a sum of vastly different initial conditions [see Eq. (26)] for the electronic mapping variables and thus subsequent nuclear dynamics. Therefore, we omit any further study of spin-PLDM beyond the population dynamics and the averaged contributions to the correlation function itself (to be discussed later in Fig. 7). However, an analysis of trajectory-converged nuclear quantities from different initial electronic conditions given by Eq. (26) would be interesting and will be the subject of future work by us.

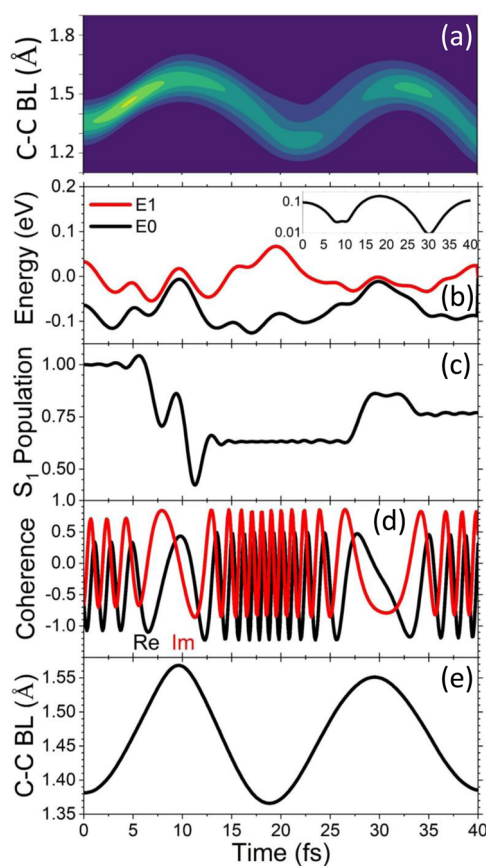


FIG. 4. (a) Fulvene C–C (ring carbon–methyl carbon) bond length density/wavepacket, composed of the same spin-LSC trajectories as provided in the construction of Fig. 3(c). (b)–(e) Observables of a single representative trajectory, including time-dependent (b) energies of the S_0 (black) and S_1 (red) electronic adiabatic states, (c) population of initially populated S_1 state, (d) real (black) and imaginary (red) S_0/S_1 electronic coherence, and (e) C–C bond length. The inset of panel (b) shows the energy difference between S_1 and S_0 on a log scale.

Figure 4(a) shows the probability density for the C–C bond stretching coordinate of the 1000-trajectory spin-LSC simulation of the fulvene molecule. The nuclear density (wavepacket) oscillates, and the system encounters the CI at each maximal value of stretching. At long times, the wavepacket broadens slightly but not by an appreciable amount since the C–C bond is never broken. During the simulation, only two oscillations of this bond are allowed. Figures 4(b)–4(e) present the result from a single trajectory of the fulvene dynamics, showing the energies of the S_1 (red) and S_0 (black) adiabatic states, the population of the S_1 state, the real (black) and imaginary (red) parts of the coherence, and the single-trajectory C–C bond stretching coordinate, respectively. The potential energy landscape through time is indicative of the prolonged nonadiabatic region analogous to Tully model No. 3 and correlates with the extended C–C bond length occurring at 10 and 30 fs. The inset of Fig. 4(b) shows the energy difference of the S_1 and S_0 states on a log scale.

The population dynamics for this trajectory showcase the complicated nonadiabatic event at 10 fs, which all mapping approaches fail to capture correctly once averaged over the 1000 trajectories. While the single trajectory population does not match the AIMS result in magnitude of population, it shows the qualitative structure (a short plateau/recurrence in S_1 population) of the AIMS result at 10 fs, which becomes absent upon trajectory-average. Furthermore, the dynamical evolution of S_1/S_0 coherence is readily available from the spin-LSC approach and correctly indicates the regions of the strong coupling by the dynamic oscillation frequency primarily dictated by the inverse of the energy difference of the electronic states.

Figure 5 shows the population dynamics of the 1,2-dithiane molecule upon excitation to the S_1 state. This model showcases an extended CI between S_1 and S_0 , which manifests as the S-S bond breaks. Periodically, roughly every 300 fs, the S-S bond reforms and thus moves the system away from the CI region. During this time (starting from ~ 30 fs), the energies of the S_1 and S_0 state are degenerate for about 100 fs [see **Fig. 6(b)**]. For this case, the AIMS results are obtained with a limited set of initial configurations (see the Appendix and **Fig. 8** for discussions). Instead of comparing with AIMS, we present the results obtained from dTSH (orange), γ -SQC- Δ (red), spin-LSC (blue), and spin-PLDM (black) approaches. We want to make clear that no single MQC result provided in **Fig. 5** is to be interpreted as more accurate than another. We provide such a comparison between these MQC approaches in hopes that future quantum dynamics approaches can use these results for comparison and benchmark.

At small times (less than 30 fs), during which the S-S bond is breaking, dTSH, γ -SQC- Δ , and spin-LSC exhibit negligible population transfer dynamics from S_1 to S_0 , while spin-PLDM shows a slight increase (above 1.0) in S_1 population. Near ~ 30 fs, when the S-S bond breaks, all MQC approaches exhibit a large decrease in S_1 population. The dTSH approach, however, quickly slows down its population transfer to the S_0 state near ~ 41 fs, while the other three approaches smoothly continue to transfer all but 20% of their

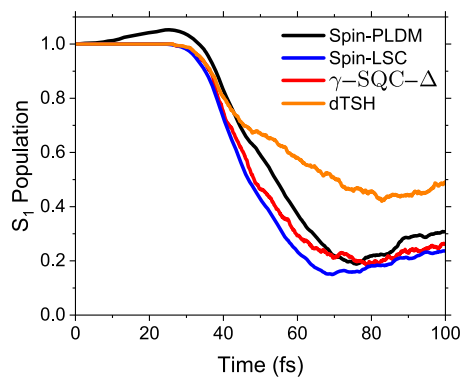


FIG. 5. S_1 population dynamics of the 1,2-dithiane molecule for a variety of semi-classical methods: spin-LSC (blue), spin-PLDM (black), γ -SQC- Δ (red), and dTSH (orange). The dTSH results were calculated using the standard SHARC code.⁹⁴ We refer the reader to the Appendix and **Fig. 8** for additional discussions regarding the available AIMS result, which prevented a rigorous comparison for this molecule.

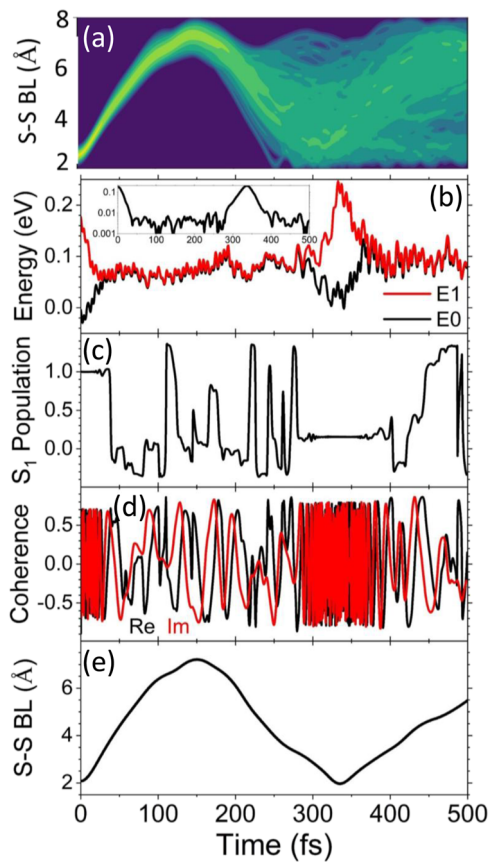


FIG. 6. (a) 1,2-dithiane S-S bond length density/wavepacket, complementary to the data in **Fig. 5(c)**. (b)–(e) Observables of a single representative trajectory, including time-dependent (b) energies of the S_0 (black) and S_1 (red) electronic adiabatic states, (c) population of initially populated S_1 state, (d) real (black) and imaginary (red) S_0/S_1 electronic coherence, and (e) S-S bond length. The inset of panel (b) shows the energy difference between S_1 and S_0 on a log scale. It is important to note that only 200 trajectories were used in the construction of panel (a) and with a larger time step of $dt = 0.5$ fs due to the computational cost of the extended time scale of 500 fs compared to 100 fs shown in **Fig. 5**.

S_1 population before rising again. To provide a consistent comparison, dTSH results shown here were simulated using the standard SHARC package⁹⁴ with 1000 trajectories and the same nuclear initial conditions as used in the other mapping-based approaches. The dTSH results may differ from the other MQC methods since it uses an adiabatic force rather than a mean-field force on the nuclei. In this case, non-adiabatic transitions (i.e., hopping) between S_0 and S_1 may exhibit drastically different forces on the nuclei.

In a similar fashion as for the fulvene molecule, in **Fig. 6**, we present a closer look at the nuclear dynamics of 1,2-dithiane for the spin-LSC approach as well as quantities from a single-trajectory. **Figure 6(a)** shows the density of the S-S bond length across 200 trajectories at an extended time scale of 500 fs. Note that **Fig. 5** only shows results up to 100 fs due to the limited AIMS data and the cost of 1000 trajectories. Analogously to the C-C bond length density shown in **Fig. 4(a)**, the S-S bond breaks ~ 2.5 Å \rightarrow 7 Å and

allows the nuclear wavepacket to broaden due to the larger conformational space. The potential energies of a single trajectory are shown in Fig. 6(b) and clearly showcase the extended degeneracy [see the inset of panel (b)] of the ground and first excited states, starting from ~30 fs until ~300 fs when the S–S bond is reforming [see the single-trajectory S–S bond length in Fig. 6(e)]. The population of the excited state is shown in Fig. 6(c) along with the coherences in Fig. 6(d). The population varies rapidly between the ground and excited states (often going above 1.0 and below 0.0) during the regions of degeneracy (30–300 fs) and implies that, unlike the fulvene molecule, substantial trajectory averaging is required for the 1,2-dithiane system in order to make any prediction regarding the populations due to the strong and prolonged coupling between the states. Similarly, the coherence showcases equally complicated behavior in and out of the regions of degeneracy.

While the results of the spin-PLDM approach in these *ab initio* test cases did not provide superior accuracy compared to SH, SQC, or spin-LSC methods, it is worthwhile to take a closer look at the spin-PLDM correlation function to better understand the approach, especially given that the PLDM approach usually provides more accurate dynamics in system–bath type of models.⁷⁹ Figure 7 presents the partial contributions $P_{\lambda\lambda'}$ to the total spin-PLDM correlation function $C_{AB} = \sum_{\lambda\lambda'} P_{\lambda\lambda'}$ [Eq. (26)] for all four molecular models explored in this work. The total spin-PLDM correlation function requires a summation of overall possible initially focused conditions $\{\lambda, \lambda'\}$ of the electronic mapping variables $\{\mathcal{Z}, \mathcal{Z}'\}$, leading to N^2 initial conditions that need to be converged with respect to the number of trajectories ($1000 \times N^2 = 4000$ trajectories in this work).

Figure 7(a) shows the population of the excited state for the AIMS result (blue) as well as the total spin-PLDM correlation function (orange). The dotted lines represent the partial contributions

to the spin-PLDM correlation function. The green dotted line is the case where $(\lambda, \lambda') = (1, 1)$ and hence has an initial value of 1.00 since this was the intended initial photo-excitation of the system. This condition appears only in the definition of the operator $\hat{A} = |1\rangle\langle 1|$, which is, in principle, not implemented until after all N^2 simulations are completed in the post-processing by explicitly performing the trace $\text{Tr}[\hat{A}\hat{w}^\dagger(\mathcal{Z}', t)\hat{B}\hat{w}(\mathcal{Z}, t)]$ once the time-dependent kernels are known for each (λ, λ') condition. The other components cannot start with any other value than 0.0 at the initial time but can accumulate population at later times, as pointed out in Refs. 64 and 65. In this model, only the off-diagonal initial conditions $(\lambda, \lambda') = (0, 1), (1, 0)$ appreciably contribute to the total population. At the final time, together they contribute up to 5.0% of the total population.

For fulvene in Fig. 7(b), a similar trend emerges where the off-diagonal initial conditions generate the most population contribution, while the diagonal initial condition (i.e., P_{00}) does not. These trends apply to the final two molecular models as well. However, the off-diagonal contributions in the latter two molecules, $[\text{CH}_2\text{NH}_2]^+$ and 1,2-dithiane, at long times, are negative, thereby diminishing the population generated by the P_{11} contribution. In fact, the off-diagonal contributions present in the $[\text{CH}_2\text{NH}_2]^+$ and 1,2-dithiane dynamics represent up to 20% and 10% at a long time. Furthermore, the ethylene and fulvene molecules exhibit periodic-like contributions from the off-diagonal initial conditions, while the other two showcase non-periodic population dynamics. It was expected that the ethylene and $[\text{CH}_2\text{NH}_2]^+$ partial contributions would look similar to one another due to the similarity of the non-adiabatic event present in each molecule, but this was not observed.

For systems with many electronic states, the number of trajectories required to converge all the partial contributions can become unmanageable. Thus, one needs to resort to approximations for the

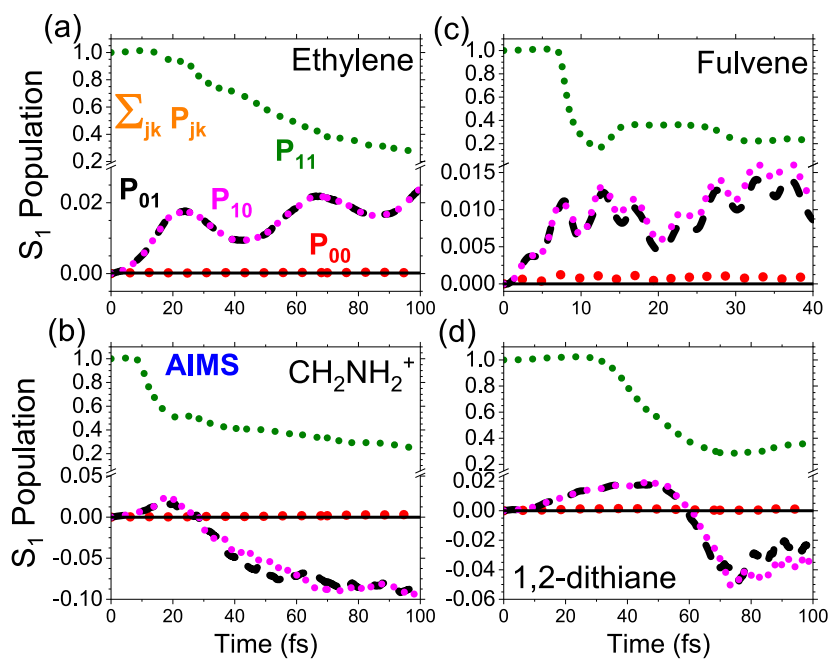


FIG. 7. S_1 population dynamics for all atomistic models, (a) ethylene, (b) $[\text{CH}_2\text{NH}_2]^+$, (c) fulvene, and (d) 1,2-dithiane, using the spin-PLDM method. The thick solid lines are the same data for AIMS (blue) and spin-PLDM (orange) in previous figures for comparison. The dotted curves showcase the partial components $P_{\lambda\lambda'}$ of the spin-PLDM correlation function for the population—a single (λ, λ') term in the sum in Eq. (26)—which decomposes each of the $N^2 = 4$ initially focused conditions of the electronic density matrix. The AIMS (blue, when available) and sum of the spin-PLDM (orange) are the same data as shown in Figs. 1–3 and 5.

simulations. We found that the spin-PLDM correlation function can be adequately represented by two approximations of the total correlation function by ignoring some of the partial contributions. The first approximation is to simply ignore all contributions except the initially excited population element $(\lambda, \lambda') = (\sigma, \sigma)$ [see discussion near Eqs. (18) and (30)]. In each of our models in this work, that amounts to keeping only the $P_{\sigma\sigma} = P_{11}$ contribution. In the *ab initio* models explored, the P_{11} population represents at least 88% of the total contribution, at worst.

The next best approximation is to add the populations from a single column of the density matrix that includes this initial excitation, i.e., $P_{\sigma\lambda}$, with twice the weight. In other words, the approximation amounts to $P_{\text{Spin-PLDM}} \approx P_{\sigma\sigma} + \sum_{\lambda \neq \sigma} 2P_{\sigma\lambda}$. Here, the factor 2 accounts for the nearly equal contribution from both the $P_{\sigma\lambda}$ and $P_{\lambda\sigma}$ terms (as shown in Fig. 7 since $P_{01} \approx P_{10}$). This approximation amounts to only N converged initial conditions instead of N^2 as prescribed by the total correlation function.

Neglecting the other diagonal initial conditions is corroborated by the results of the main text, where P_{00} never contributed any appreciable amount of population. The other off-diagonal initial conditions $P_{\lambda\lambda'}$, where $\lambda \neq \sigma$ and $\lambda' \neq \sigma$, require an examination of a system with more than two electronic states. Figure S1 of the supplementary material presents the population dynamics for the FMO 7-state model system,^{64,65} which has been previously studied with spin-PLDM and achieves superior accuracy compared to FSSH, SQC, and spin-LSC, matching the benchmark hierarchical equations of motion (HEOM) result. Figure S2a presents the partial contributions to the ground state S_0 population as well as the single-column approximation, which yields the same accuracy as the full spin-PLDM correlation function result with seven converged simulations instead of 49, a reduction of 86% in computational cost. The other diagonal and off-diagonal initial conditions are shown in Figs. S2(b) and S2(c) and show less than 0.3% contribution at all times. We hypothesize that drastic reductions in cost can be achieved for more complicated situations than population dynamics, such as those in non-linear spectra,^{102,103} where similar arguments can be made to neglect certain elements of the initial conditions.

IV. CONCLUSIONS

In this work, we use the quasi-diabatic propagation scheme^{78,82,83} to directly interface the diabatic linearized (spin-LSC)^{28,63,66} and partially linearized (spin-PLDM) spin-mapping approaches^{64,65} and the CASSCF on-the-fly electronic structure calculations to propagate *ab initio* non-adiabatic dynamics. We have performed on-the-fly simulations for four recently investigated molecules: ethylene, fulvene, methyliminium cation (CH_2NH_2^+), and 1,2-dithiane.^{73,88–90} These molecular models provide examples of common non-adiabatic phenomena found ubiquitously in realistic systems, namely conical interactions and avoided crossings, and are closely related to the well-known simple curve crossing models of Tully.¹

We have shown that all MQC methods provide qualitatively correct population dynamics when comparing to *ab initio* multiple spawning (AIMS).^{73,88–90} In all cases, spin-LSC exhibits a similar level of accuracy (almost quantitatively) to the recently developed symmetric quasi-classical (SQC) approach with a trajectory-adjusted zero-point energy parameter.²⁷ Various flavors of trajectory

surface hopping (TSH) are qualitatively similar to the other MQC approaches used in this work, showing major differences only in the more complicated 1,2-dithiane molecular model. Although we expected the more involved spin-PLDM approach to exhibit superior accuracy compared to the spin-LSC method, which was previously shown for system–bath type models (see Figs. S1 and S2 of the supplementary material), we found that neither method was consistently more accurate than the other when compared to the AIMS result. However, we note that recent studies have shown⁷³ that AIMS itself is not always guaranteed to provide *quality* benchmark results and are often difficult to converge due to the poor scaling of the spawning algorithm. So, the minor deviations between the various MQC approaches pointed out in this work must be carefully weighed against the proposed quality of the benchmark.

We also note that while we expected spin-PLDM to provide superior results,^{64,65,102} recent work has explored the short-time accuracy (through low-order time-derivatives of the estimators evaluated at the initial time) of the spin-LSC and spin-PLDM approaches to reveal that for arbitrary two-state scattering systems, spin-PLDM provides no improvement over spin-LSC.⁷⁰ However, for spin-boson type problems, such as the FMO complex (which contains only a linear force) in Figs. S1 and S2 of the supplementary material, even for a two-state case, spin-PLDM should provide a more accurate answer,⁷⁰ which is also the case for a standard PLDM approach.⁷

We further explored the nature of the spin-PLDM correlation function by examining the various components (initially focused contributions λ and λ') individually. Here, we noted that when calculating an initial population element $|\sigma\rangle\langle\sigma|$, the off-diagonal initially focused conditions $P_{\sigma\lambda}$ (where $\lambda \neq \sigma$) contribute nearly the same magnitude and sign to the overall correlation function as $P_{\lambda\sigma}$. Thus, calculating one and doubling its weight provides the same contribution to the total correlation function. Furthermore, the other diagonal contributions $P_{\lambda\lambda}$ (with $\lambda \neq \sigma$) have minimal magnitude in their contribution to the overall correlation function and can be ignored. In this sense, an approximate scheme can be constructed, at least in these few example systems explored in this work. In this case, one only needs to calculate a single column of initially focused density matrix elements, which reduces the computational cost from N^2 to N converged simulations. Note that this still amounts to more computations than the spin-LSC approach, which only ever requires one converged initial condition given an initial excitation to $|\sigma\rangle\langle\sigma|$.

These calculations provide valuable and non-trivial tests to systematically investigate the numerical performance of various recently developed quantum dynamics approaches, going beyond the simple diabatic model systems that have historically been the major workhorses in the quantum dynamics field. At the same time, we hope that these results will serve as useful benchmarks in future studies and will foster the development of new quantum dynamics approaches.

SUPPLEMENTARY MATERIAL

See the supplementary material for details about the computational details of the model simulations and additional results of dynamics in model systems.

ACKNOWLEDGMENTS

This work was supported by the National Science Foundation Award under Grant No. CHE-2244683. The software development in this work was supported by the National Science Foundation's Office of Advanced Cyber-infrastructure under Award No. OAC-2311442. D.H. was supported by the Beijing Natural Science Foundation (Grant No. 2244074) and the start-up funding (Grant No. 312200502511) from Beijing Normal University at Zhuhai. A.M. was supported by the Texas A & M Department of Chemistry Startup Fund. Computing resources were provided by the Center for Integrated Research Computing (CIRC) at the University of Rochester. The authors thank Wenxiang Ying for providing the HEOM benchmark data for the model systems and Lea M. Ibele for helpful discussions regarding the AIMS benchmark results. We also thank both reviewers for their valuable and detailed feedback on this paper.

AUTHOR DECLARATIONS

Conflict of Interest

The authors have no conflicts to disclose.

Author Contributions

Braden M. Weight: Conceptualization (equal); Data curation (lead); Formal analysis (lead); Investigation (lead); Methodology (lead); Software (lead); Validation (lead); Visualization (lead); Writing – original draft (lead); Writing – review & editing (equal). **Arkajit Mandal:** Conceptualization (equal); Formal analysis (equal); Funding acquisition (equal); Investigation (equal); Methodology (equal); Project administration (equal); Resources (equal); Software (equal); Supervision (equal); Validation (equal); Writing – original draft (equal); Writing – review & editing (equal). **Deping Hu:** Conceptualization (equal); Data curation (equal); Formal analysis (equal); Validation (equal); Visualization (equal); Writing – original draft (supporting). **Pengfei Huo:** Conceptualization (equal); Funding acquisition (lead); Methodology (equal); Project administration (lead); Supervision (lead); Writing – original draft (equal); Writing – review & editing (lead).

DATA AVAILABILITY

The data that support the findings of this study are available from the corresponding author upon reasonable request.

APPENDIX: INITIAL CONDITIONS AND CONVERGENCE OF POPULATION DYNAMICS

The comparison between the trajectory-based approaches and AIMS for the 1,2-dithiane molecular species (Fig. 5) was significantly worse than the other molecular models. While this discrepancy could be at least partially attributed to the quality of the MQC approaches and the complexity of the 1,2-dithiane dynamics of an extended region of degeneracy between the ground and excited states, we briefly examine the quality and robustness of the initial conditions of the original AIMS data provided in Ref. 90.

In the original work,⁹⁰ the authors used 14 unique initial nuclear geometries and nuclear momentum sampled from the Wigner distribution for their AIMS and dTSH calculations. Furthermore, the authors repeated these 14 nuclear samples eight times with different random seeds for a total of 112 trajectories to converge their approach, which is inherently stochastic similar to the standard TSH approach. A major limitation of these results is the limited amount of the position/momenta sampled at initial time. These limited numbers of nuclear samples were chosen due to the large computational cost of the AIMS dynamics simulations. However, to understand the large discrepancies between the AIMS results and MQC populations, we explore the dependence of the spin-LSC results on the reduced initial nuclear sampling identical to that of the original AIMS initial conditions.

Using the same 14 nuclear geometries and nuclear momenta provided in the supplementary material of Ref. 90, we performed spin-LSC dynamics on the 1,2-dithiane molecular system to compare to the fully converged spin-LSC under various conditions. First, we used the 14 nuclear samples to perform only 14 trajectories (each with individually sampled electronic mapping variables), which we denote as (14n, 1e) to imply 14 unique nuclear samples repeated 1× (which does not converge the electronic sampling per nuclear sample nor on the average). Second, we used the 14 nuclear samples repeated 30 times with different electronic samplings for a total of 420 trajectories, which we denote as (14n, 30e). Finally, we replot the fully converged calculations shown in the main text [see Fig. 5(c)], which, using the notation introduced here, is (1000n, 1e) for a total of 1000 trajectories.

Figure 8 shows the S_1 population dynamics for each of the cases outlined above as well as the AIMS result (blue solid line), with (14n, 1e) shown as an orange thin solid line, (14n, 30e) shown as an orange dotted line, and (1000n, 1e) shown as an orange thick transparent line. Notably, the (14n, 1e) results closely match the

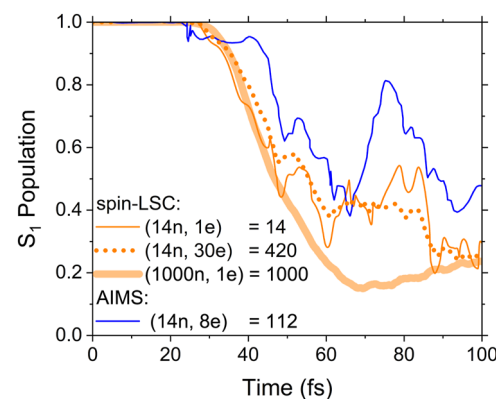


FIG. 8. S_1 population dynamics of the 1,2-dithiane molecular model for the spin-LSC (orange curves) and AIMS (blue curve) approaches. To more directly compare the spin-LSC method to the benchmark AIMS result (data taken from Ref. 90), the spin-LSC was performed using the same 14 initial geometry/momenta as used in and provided by Ref. 90 using a single electronic sampling per nuclear configuration (14n, 1e) (orange thin solid line) and 30 electronic samplings per nuclear configuration (14n, 30e) (orange dotted line). The 1000-sample spin-LSC (1000n, 1e) (orange thick solid line) and the 14-sample AIMS (14n, 8e) (blue line) are identical to the data provided in Fig. 5(c).

trends seen in the AIMS population curve, especially at the population recurrence times near 45, 55, and 80 fs, thus showing that the spin-LSC approach and the AIMS approach are qualitatively similar given the same/similar initial conditions. The (14n, 30e) results, which represent convergence only on the electronic DOFs for the given initial nuclear samples, showcase a very similar trend as the (14n, 1e) but slightly smoother with less rapid changes in population. Finally, we note that the fully converged case (1000n, 1e) bears little resemblance to any of the other curves and is significantly smoother. This exemplifies the fact that the sharp edges/shoulders shown in the AIMS result (and the other non-converged spin-LSC results) are artifacts of the limited nuclear samples provided, thus showing the strong dependence of the limited nuclear configurations on the results.

While the AIMS approach is, in principle, a rigorous path toward the exact dynamics of photo-excited molecular systems, the computational cost of this approach sometimes forces the user to relax the parameters necessary for convergence, especially for the number of initial Gaussian functions. In a similar vein, it has recently been pointed out that AIMS may not always capture the correct non-adiabatic physics in certain molecular systems, even for fully converged initial conditions, and that independent trajectory MQC simulations may provide a more quantitative result in these cases.⁷³ We suggest caution when using such results for a benchmark against more approximate methods such as novel MQC approaches. Thus, care must be taken when comparing the MQC results to these high-level benchmarks, keeping in mind that the convergence of the parameters/initial conditions for these wavepacket approaches is paramount to the quality of the results.

REFERENCES

- ¹J. C. Tully, "Molecular dynamics with electronic transitions," *J. Chem. Phys.* **93**(2), 1061–1071 (1990).
- ²M. Ben-Nun, J. Quenneville, and T. J. Martínez, "Ab initio multiple spawning: Photochemistry from first principles quantum molecular dynamics," *J. Phys. Chem. A* **104**(22), 5161–5175 (2000).
- ³D. A. Micha, "Time-dependent many-electron treatment of electronic energy and charge transfer in atomic collisions," *J. Phys. Chem. A* **103**(38), 7562–7574 (1999).
- ⁴S. Bonella and D. F. Coker, "A semiclassical limit for the mapping Hamiltonian approach to electronically nonadiabatic dynamics," *J. Chem. Phys.* **114**(18), 7778–7789 (2001).
- ⁵G. A. Worth, M. A. Robba, and I. Burghardt, "A novel algorithm for non-adiabatic direct dynamics using variational Gaussian wavepackets," *Faraday Discuss.* **127**, 307–323 (2004).
- ⁶N. Ananth, C. Venkataraman, and W. H. Miller, "Semiclassical description of electronically nonadiabatic dynamics via the initial value representation," *J. Chem. Phys.* **127**, 084114 (2007).
- ⁷P. Huo and D. F. Coker, "Communication: Partial linearized density matrix dynamics for dissipative, non-adiabatic quantum evolution," *J. Chem. Phys.* **135**(20), 201101 (2011).
- ⁸F. Plasser, G. Granucci, J. Pittner, M. Barbatti, M. Persico, and H. Lischka, "Surface hopping dynamics using a locally diabatic formalism: Charge transfer in the ethylene dimer cation and excited state dynamics in the 2-pyridone dimer," *J. Chem. Phys.* **137**(22), 22A514 (2012).
- ⁹K. Saita and D. V. Shalashilin, "On-the-fly ab initio molecular dynamics with multiconfigurational Ehrenfest method," *J. Chem. Phys.* **137**, 22A506 (2012).
- ¹⁰D. V. Makhov, W. J. Glover, T. J. Martinez, and D. V. Shalashilin, "Ab initio multiple cloning algorithm for quantum nonadiabatic molecular dynamics," *J. Chem. Phys.* **141**(5), 054110 (2014).
- ¹¹S. J. Cotton and W. H. Miller, "Symmetrical windowing for quantum states in quasi-classical trajectory simulations: Application to electronically non-adiabatic processes," *J. Chem. Phys.* **139**, 234112 (2013).
- ¹²S. J. Cotton and W. H. Miller, "Symmetrical windowing for quantum states in quasi-classical trajectory simulations," *J. Phys. Chem. A* **117**(32), 7190–7194 (2013).
- ¹³N. Ananth, "Mapping variable ring polymer molecular dynamics: A path-integral based method for nonadiabatic processes," *J. Chem. Phys.* **139**(12), 124102 (2013).
- ¹⁴C.-Y. Hsieh and R. Kapral, "Analysis of the forward-backward trajectory solution for the mixed quantum-classical Liouville equation," *J. Chem. Phys.* **138**(13), 134110 (2013).
- ¹⁵J. O. Richardson and M. Thoss, "Communication: Nonadiabatic ring-polymer molecular dynamics," *J. Chem. Phys.* **139**, 031102 (2013).
- ¹⁶A. R. Menzelev, F. Bell, and T. F. Miller III, "Kinetically constrained ring-polymer molecular dynamics for non-adiabatic chemical reactions," *J. Chem. Phys.* **140**(6), 064103 (2014).
- ¹⁷G. A. Meek and B. G. Levine, "Evaluation of the time-derivative coupling for accurate electronic state transition probabilities from numerical simulations," *J. Phys. Chem. Lett.* **5**, 2351–2356 (2014).
- ¹⁸J. E. Subotnik, A. Jain, B. Landry, A. Petit, W. Ouyang, and N. Bellonzi, "Understanding the surface hopping view of electronic transitions and decoherence," *Annu. Rev. Phys. Chem.* **67**, 387–417 (2016).
- ¹⁹T. Nelson, A. Naumov, S. Fernandez-Alberti, and S. Tretiak, "Nonadiabatic excited-state molecular dynamics: On-the-fly limiting of essential excited states," *Chem. Phys.* **481**, 84–90 (2016).
- ²⁰A. Jain, E. Alguire, and J. E. Subotnik, "An efficient, augmented surface hopping algorithm that includes decoherence for use in large-scale simulations," *J. Chem. Theory Comput.* **12**, 5256–5268 (2016).
- ²¹P. L. Walters and N. Makri, "Iterative quantum-classical path integral with dynamically consistent state hopping," *J. Chem. Phys.* **144**, 044108 (2016).
- ²²S. Pal, D. J. Trivedi, A. V. Akimov, B. Aradi, T. Frauenheim, and O. V. Prezhdo, "Nonadiabatic molecular dynamics for thousand atom systems: A tight-binding approach toward PYXAID," *J. Chem. Theory Comput.* **12**(4), 1436–1448 (2016).
- ²³S. N. Chowdhury and P. Huo, "Coherent state mapping ring polymer molecular dynamics for non-adiabatic quantum propagations," *J. Chem. Phys.* **147**, 214109 (2017).
- ²⁴B. F. E. Curchod and T. J. Martínez, "Ab initio nonadiabatic quantum molecular dynamics," *Chem. Rev.* **118**, 3305–3336 (2018).
- ²⁵R. Crespo-Otero and M. Barbatti, "Recent advances and perspectives on nonadiabatic mixed quantum-classical dynamics," *Chem. Rev.* **118**, 7026–7068 (2018).
- ²⁶E. Mulvihill, A. Schubert, X. Sun, B. D. Dunietz, and E. Geva, "A modified approach for simulating electronically nonadiabatic dynamics via the generalized quantum master equation," *J. Chem. Phys.* **150**, 034101 (2019).
- ²⁷S. J. Cotton and W. H. Miller, "Trajectory-adjusted electronic zero point energy in classical Meyer-Miller vibronic dynamics: Symmetrical quasiclassical application to photodissociation," *J. Chem. Phys.* **150**, 194110 (2019).
- ²⁸J. E. Runeson and J. O. Richardson, "Generalized spin mapping for quantum-classical dynamics," *J. Chem. Phys.* **152**(8), 084110 (2020).
- ²⁹B. F. E. Curchod and F. Agostini, "On the dynamics through a conical intersection," *J. Phys. Chem. Lett.* **8**(4), 831–837 (2017).
- ³⁰F. Agostini and B. F. E. Curchod, "Different flavors of nonadiabatic molecular dynamics," *Wiley Interdiscip. Rev.: Comput. Mol. Sci.* **9**(5), e1417 (2019).
- ³¹L. M. Ibele, E. Sangiogo Gil, B. F. E. Curchod, and F. Agostini, "On the nature of geometric and topological phases in the presence of conical intersections," *J. Phys. Chem. Lett.* **14**(51), 11625–11631 (2023).
- ³²T. R. Nelson, A. J. White, J. A. Bjorgaard, A. E. Sifain, Y. Zhang, B. Neogen, S. Fernandez-Alberti, D. Mozyrsky, A. E. Roitberg, and S. Tretiak, "Non-adiabatic excited-state molecular dynamics: Theory and applications for modeling photophysics in extended molecular materials," *Chem. Rev.* **120**(4), 2215–2287 (2020).
- ³³Y. Zhang, L. Li, S. Tretiak, and T. Nelson, "Nonadiabatic excited-state molecular dynamics for open-shell systems," *J. Chem. Theory Comput.* **16**(4), 2053–2064 (2020).

- ³⁴Y. Zhang, T. Nelson, and S. Tretiak, "Non-adiabatic molecular dynamics of molecules in the presence of strong light-matter interactions," *J. Chem. Phys.* **151**(15), 154109 (2019).
- ³⁵N. M. Hoffmann, H. Appel, A. Rubio, and N. T. Maitra, "Light-matter interactions via the exact factorization approach," *Eur. Phys. J. B* **91**(8), 180 (2018).
- ³⁶T. Nelson, S. Fernandez-Alberti, A. E. Roitberg, and S. Tretiak, "Nonadiabatic excited-state molecular dynamics: Treatment of electronic decoherence," *J. Chem. Phys.* **138**(22), 224111 (2013).
- ³⁷V. M. Freixas, A. J. White, T. Nelson, H. Song, D. V. Makhov, D. Shalashilin, S. Fernandez-Alberti, and S. Tretiak, "Nonadiabatic excited-state molecular dynamics methodologies: Comparison and convergence," *J. Phys. Chem. Lett.* **12**(11), 2970–2982 (2021).
- ³⁸V. M. Freixas, W. Malone, X. Li, H. Song, H. Negrin-Yuvero, R. Pérez-Castillo, A. White, T. R. Gibson, D. V. Makhov, D. V. Shalashilin, Y. Zhang, N. Fedik, M. Kulichenko, R. Messerly, L. N. Mohanam, S. Sharifzadeh, A. Bastida, S. Mukamel, S. Fernandez-Alberti, and S. Tretiak, "NEXMD v2.0 software package for nonadiabatic excited state molecular dynamics simulations," *J. Chem. Theory Comput.* **19**, 5356 (2023).
- ³⁹J. C. Tully, "Perspective: Nonadiabatic dynamics theory," *J. Chem. Phys.* **137**(22), 22A301 (2012).
- ⁴⁰G. Kab, "Mean field Ehrenfest quantum/classical simulation of vibrational energy relaxation in a simple liquid," *Phys. Rev. E* **66**, 046117 (2002).
- ⁴¹P. V. Parandekar and J. C. Tully, "Detailed balance in Ehrenfest mixed quantum-classical dynamics," *J. Chem. Theory Comput.* **2**(2), 229–235 (2006).
- ⁴²A. Abedi, N. T. Maitra, and E. K. U. Gross, "Exact factorization of the time-dependent electron-nuclear wave function," *Phys. Rev. Lett.* **105**(12), 123002 (2010).
- ⁴³J.-K. Ha and S. K. Min, "Independent trajectory mixed quantum-classical approaches based on the exact factorization," *J. Chem. Phys.* **156**(17), 174109 (2022).
- ⁴⁴P. Vindel-Zandbergen, S. Matsika, and N. T. Maitra, "Exact-factorization-based surface hopping for multistate dynamics," *J. Phys. Chem. Lett.* **13**(7), 1785–1790 (2022).
- ⁴⁵D. Han, J.-K. Ha, and S. K. Min, "Real-space and real-time propagation for correlated electron–nuclear dynamics based on exact factorization," *J. Chem. Theory Comput.* **19**, 2186 (2023).
- ⁴⁶L. Dupuy, A. Rikus, and N. T. Maitra, "Exact-factorization-based surface hopping without velocity adjustment," *J. Phys. Chem. Lett.* **15**(10), 2643–2649 (2024).
- ⁴⁷S. K. Min, F. Agostini, and E. K. U. Gross, "Coupled-trajectory quantum-classical approach to electronic decoherence in nonadiabatic processes," *Phys. Rev. Lett.* **115**(7), 073001 (2015).
- ⁴⁸S. K. Min, F. Agostini, I. Tavernelli, and E. K. U. Gross, "Ab initio nonadiabatic dynamics with coupled trajectories: A rigorous approach to quantum (De)coherence," *J. Phys. Chem. Lett.* **8**(13), 3048–3055 (2017).
- ⁴⁹F. Agostini, S. K. Min, A. Abedi, and E. K. U. Gross, "Quantum-classical nonadiabatic dynamics: Coupled- vs independent-trajectory methods," *J. Chem. Theory Comput.* **12**(5), 2127–2143 (2016).
- ⁵⁰P. Huo and D. F. Coker, "Semi-classical path integral non-adiabatic dynamics: A partial linearized classical mapping Hamiltonian approach," *Mol. Phys.* **110**(9–10), 1035–1052 (2012).
- ⁵¹S. N. Chowdhury and P. Huo, "State dependent ring polymer molecular dynamics for investigating excited nonadiabatic dynamics," *J. Chem. Phys.* **150**, 244102 (2019).
- ⁵²S. N. Chowdhury, A. Mandal, and P. Huo, "Ring polymer quantization of the photon field in polariton chemistry," *J. Chem. Phys.* **154**, 044109 (2021).
- ⁵³S. N. Chowdhury and P. Huo, "Non-adiabatic Matsubara dynamics and non-adiabatic ring-polymer molecular dynamics," *J. Chem. Phys.* **154**, 124124 (2021).
- ⁵⁴D. L. Bossion, S. N. Chowdhury, and P. Huo, "Non-adiabatic ring polymer molecular dynamics in the phase space of the SU(N) Lie group," *J. Chem. Phys.* **158**, 084105 (2023).
- ⁵⁵R. Lambert and N. Makri, "Quantum-classical path integral. I. Classical memory and weak quantum nonlocality," *J. Chem. Phys.* **137**(22), 22A552 (2012).
- ⁵⁶R. Lambert and N. Makri, "Quantum-classical path integral. II. Numerical methodology," *J. Chem. Phys.* **137**(22), 22A553 (2012).
- ⁵⁷T. Banerjee and N. Makri, "Quantum-classical path integral with self-consistent solvent-driven reference propagators," *J. Phys. Chem. B* **117**(42), 13357–13366 (2013).
- ⁵⁸N. Makri, "Quantum-classical path integral: A rigorous approach to condensed phase dynamics," *Int. J. Quantum Chem.* **115**(18), 1209–1214 (2015).
- ⁵⁹C.-Y. Hsieh and R. Kapral, "Nonadiabatic dynamics in open quantum-classical systems: Forward-backward trajectory solution," *J. Chem. Phys.* **137**(22), 22A507 (2012).
- ⁶⁰S. J. Cotton, R. Liang, and W. H. Miller, "On the adiabatic representation of Meyer-Miller electronic-nuclear dynamics," *J. Chem. Phys.* **147**(6), 064112 (2017).
- ⁶¹S. J. Cotton and W. H. Miller, "A new symmetrical quasi-classical model for electronically non-adiabatic processes: Application to the case of weak non-adiabatic coupling," *J. Chem. Phys.* **145**(14), 144108 (2016).
- ⁶²S. J. Cotton and W. H. Miller, "A symmetrical quasi-classical windowing model for the molecular dynamics treatment of non-adiabatic processes involving many electronic states," *J. Chem. Phys.* **150**(10), 104101 (2019).
- ⁶³J. E. Runeson and J. O. Richardson, "Spin-mapping approach for nonadiabatic molecular dynamics," *J. Chem. Phys.* **151**(4), 044119 (2019).
- ⁶⁴J. R. Mannouch and J. O. Richardson, "A partially linearized spin-mapping approach for nonadiabatic dynamics. I. Derivation of the theory," *J. Chem. Phys.* **153**(19), 194109 (2020).
- ⁶⁵J. R. Mannouch and J. O. Richardson, "A partially linearized spin-mapping approach for nonadiabatic dynamics. II. Analysis and comparison with related approaches," *J. Chem. Phys.* **153**(19), 194110 (2020).
- ⁶⁶D. Bossion, W. Ying, S. N. Chowdhury, and P. Huo, "Non-adiabatic mapping dynamics in the phase space of the SU(N) Lie group," *J. Chem. Phys.* **157**, 084105 (2022).
- ⁶⁷X. He, B. Wu, Z. Gong, and J. Liu, "Commutator matrix in phase space mapping models for nonadiabatic quantum dynamics," *J. Phys. Chem. A* **125**(31), 6845–6863 (2021).
- ⁶⁸X. He, Z. Gong, B. Wu, and J. Liu, "Negative zero-point-energy parameter in the Meyer–Miller mapping model for nonadiabatic dynamics," *J. Phys. Chem. Lett.* **12**(10), 2496–2501 (2021).
- ⁶⁹X. He and J. Liu, "A new perspective for nonadiabatic dynamics with phase space mapping models," *J. Chem. Phys.* **151**(2), 024105 (2019).
- ⁷⁰H. Lang, O. Vendrell, and P. Hauke, "Generalized discrete truncated Wigner approximation for nonadiabatic quantum-classical dynamics," *J. Chem. Phys.* **155**(2), 024111 (2021).
- ⁷¹J. R. Mannouch and J. O. Richardson, "A mapping approach to surface hopping," *J. Chem. Phys.* **158**(10), 104111 (2023).
- ⁷²J. E. Runeson and D. E. Manolopoulos, "A multi-state mapping approach to surface hopping," *J. Chem. Phys.* **159**(9), 094115 (2023).
- ⁷³J. R. Mannouch and A. Kelly, "Quantum quality with classical cost: *Ab initio* nonadiabatic dynamics simulations using the mapping approach to surface hopping," *J. Phys. Chem. Lett.* **15**(22), 5814–5823 (2024).
- ⁷⁴G. Amati, J. R. Mannouch, and J. O. Richardson, "Detailed balance in mixed quantum–classical mapping approaches," *J. Chem. Phys.* **159**(21), 214114 (2023).
- ⁷⁵H.-D. Meyer and W. H. Miller, "A classical analog for electronic degrees of freedom in nonadiabatic collision processes," *J. Chem. Phys.* **70**(7), 3214–3223 (1979).
- ⁷⁶G. Stock and M. Thoss, "Semiclassical description of nonadiabatic quantum dynamics," *Phys. Rev. Lett.* **78**(4), 578–581 (1997).
- ⁷⁷M. Thoss and G. Stock, "Mapping approach to the semiclassical description of nonadiabatic quantum dynamics," *Phys. Rev. A* **59**, 64–79 (1999).
- ⁷⁸A. Mandal, S. S. Yamjala, and P. Huo, "Quasi-diabatic representation for non-adiabatic dynamics propagation," *J. Chem. Theory Comput.* **14**(4), 1828–1840 (2018).
- ⁷⁹A. Mandal, F. A. Shakib, and P. Huo, "Investigating photoinduced proton coupled electron transfer reaction using quasi diabatic dynamics propagation," *J. Chem. Phys.* **148**(24), 244102 (2018).
- ⁸⁰A. Mandal, J. S. Sandoval C, F. A. Shakib, and P. Huo, "Quasi-diabatic propagation scheme for direct simulation of proton-coupled electron transfer reaction," *J. Phys. Chem. A* **123**(12), 2470–2482 (2019).

- ⁸¹J. Sebastian Sandoval, A. Mandal, and P. Huo, "Symmetric quasi classical dynamics with quasi diabatic propagation scheme," *J. Chem. Phys.* **149**(4), 044115 (2018).
- ⁸²W. Zhou, A. Mandal, and P. Huo, "Quasi-diabatic scheme for nonadiabatic on-the-fly simulations," *J. Phys. Chem. Lett.* **10**(22), 7062–7070 (2019).
- ⁸³B. M. Weight, A. Mandal, and P. Huo, "*Ab initio* symmetric quasi-classical approach to investigate molecular Tully models," *J. Chem. Phys.* **155**(8), 084106 (2021).
- ⁸⁴D. Hu, A. Mandal, B. M. Weight, and P. Huo, "Quasi-diabatic propagation scheme for simulating polariton chemistry," *J. Chem. Phys.* **157**, 194109 (2022).
- ⁸⁵Y. Guan, H. Guo, and D. R. Yarkony, "Neural network based quasi-diabatic Hamiltonians with symmetry adaptation and a correct description of conical intersections," *J. Chem. Phys.* **150**(21), 214101 (2019).
- ⁸⁶X. Zhu and D. R. Yarkony, "Quasi-diabatic representations of adiabatic potential energy surfaces coupled by conical intersections including bond breaking: A more general construction procedure and an analysis of the diabatic representation," *J. Chem. Phys.* **137**(22), 22A511 (2012).
- ⁸⁷Y. Wang, C. Xie, H. Guo, and D. R. Yarkony, "A quasi-diabatic representation of the 1,2¹A states of methylamine," *J. Phys. Chem. A* **123**(25), 5231–5241 (2019).
- ⁸⁸L. M. Ibele and B. F. E. Curchod, "A molecular perspective on Tully models for nonadiabatic dynamics," *Phys. Chem. Chem. Phys.* **22**(27), 15183–15196 (2020).
- ⁸⁹P. Vindel-Zandbergen, L. M. Ibele, J.-K. Ha, S. K. Min, B. F. E. Curchod, and N. T. Maitra, "Study of the decoherence correction derived from the exact factorization approach for nonadiabatic dynamics," *J. Chem. Theory Comput.* **17**, 3852 (2021).
- ⁹⁰L. M. Ibele, Y. Lassmann, T. J. Martínez, and B. F. E. Curchod, "Comparing (stochastic-selection) *ab initio* multiple spawning with trajectory surface hopping for the photodynamics of cyclopropanone, fulvene, and dithiane," *J. Chem. Phys.* **154**(10), 104110 (2021).
- ⁹¹P. Huo, T. F. Miller III, and D. F. Coker, "Communication: Predictive partial linearized path integral simulation of condensed phase electron transfer dynamics," *J. Chem. Phys.* **139**(15), 151103 (2013).
- ⁹²M. Elious Mondal, E. R. Koessler, J. Provazza, A. N. Vamivakas, S. T. Cundiff, T. D. Krauss, and P. Huo, "Quantum dynamics simulations of the 2D spectroscopy for exciton polaritons," *J. Chem. Phys.* **159**(9), 094102 (2023).
- ⁹³M. Elious Mondal, A. Nickolas Vamivakas, S. T. Cundiff, T. D. Krauss, and P. Huo, "Polariton spectra under the collective coupling regime. I. Efficient simulation of linear spectra and quantum dynamics," *J. Chem. Phys.* **162**, 014114 (2025).
- ⁹⁴S. Mai, M. Richter, M. Heindl, M. F. S. J. Menger, A. Atkins, M. Ruckebauer, F. Plasser, L. Maria Ibele, S. Kropf, M. Oppel, P. Marquetand, and L. González, Surface Hopping, Including Arbitrary Couplings—Program Package for Non-Adiabatic Dynamics, SHARC2.1, 2019.
- ⁹⁵H.-J. Werner, P. J. Knowles, G. Knizia, F. R. Manby, and M. Schütz, "Molpro: A general-purpose quantum chemistry program package," *Wiley Interdiscip. Rev.:Comput. Mol. Sci.* **2**, 242–253 (2012).
- ⁹⁶J. P. Dahl and M. Springborg, "The Morse oscillator in position space, momentum space, and phase space," *J. Chem. Phys.* **88**, 4535–4547 (1988).
- ⁹⁷R. Schinke, *Photodissociation Dynamics: Spectroscopy and Fragmentation of Small Polyatomic Molecules* (Cambridge University Press, 1995).
- ⁹⁸D. Tannor, *Introduction to Quantum Mechanics: A Time-dependent Perspective* (University Science books Mill Valley, 2007).
- ⁹⁹G. Granucci and M. Persico, "Critical appraisal of the fewest switches algorithm for surface hopping," *J. Chem. Phys.* **126**(13), 134114 (2007).
- ¹⁰⁰G. Granucci, M. Persico, and A. Toniolo, "Direct semiclassical simulation of photochemical processes with semiempirical wave functions," *J. Chem. Phys.* **114**(24), 10608–10615 (2001).
- ¹⁰¹J. E. Subotnik and N. Shenvi, "A new approach to decoherence and momentum rescaling in the surface hopping algorithm," *J. Chem. Phys.* **134**(2), 024105 (2011).
- ¹⁰²J. R. Mannouch and J. O. Richardson, "A partially linearized spin-mapping approach for simulating nonlinear optical spectra," *J. Chem. Phys.* **156**(2), 024108 (2022).
- ¹⁰³Z. Li, J. Peng, Y. Zhu, C. Xu, M. F. Gelin, F. L. Gu, and Z. Lan, "On-the-fly simulations of transient absorption pump-probe spectra: Combining mapping dynamics with doorway-window protocol," *chemRxiv:10.26434/chemrxiv-2024-7zl3b-v4* (2024).